

1 **Susceptibility of Marine Warm Clouds to Aerosols in**  
2 **Different Monsoon Periods over the South China Sea**

3 Yan Liu<sup>1</sup>, Hailing Jia<sup>2</sup>, Yong Han<sup>1\*</sup>

4 <sup>1</sup>Advanced Science & Technology of Space and Atmospheric Physics Group (ASAG), School of  
5 Atmospheric Sciences, Sun Yat-sen University, 519082 Zhuhai, China

6 <sup>2</sup>SRON Space Research Organisation Netherlands, Leiden, The Netherlands

7 \* *Correspondence to:* Yong Han (hany66@mail.sysu.edu.cn)

8

9 **Abstract.**

10 Understanding the susceptibility of warm clouds to aerosol loading, quantified by the aerosol–cloud  
11 interactions (ACI) index, is essential for assessing ACI and their climate impacts. Previous studies have  
12 demonstrated that this susceptibility is strongly modulated by environmental conditions. The South  
13 China Sea (SCS), influenced alternately by the southwest and northeast monsoons, provides a unique  
14 natural laboratory for examining ACI under contrasting thermodynamic and moisture conditions. Using  
15 long-term satellite observations and reanalysis data, we investigate ACI in non-raining warm liquid  
16 clouds over the SCS across three monsoon phases: the southwest monsoon wet period (SWMW),  
17 northeast monsoon wet period (NEMW), and northeast monsoon dry period (NEMD). The robust  
18 Twomey effect is observed across all periods. Shallow stratocumulus clouds show no significant  
19 differences in ACI across periods, whereas deeper cumulus clouds exhibit the strongest ACI during  
20 NEMD, with no clear separation between SWMW and NEMW. The enhanced ACI during NEMD is  
21 consistent with the relatively dry and stable lower-tropospheric environment (LTS), where stable  
22 conditions may enhance ACI through aerosol accumulation, while moist environments are likely to  
23 weaken it via enhanced condensational and coalescence growth. However, these differences likely reflect  
24 co-varying environmental conditions across monsoon periods rather than a single dominant controlling  
25 factor. Limitations of AI as a marine cloud condensation nuclei (CCN) proxy and satellite retrieval biases  
26 may affect these conclusions. These findings suggest that, within a monsoon-organized framework, the  
27 interplay among aerosols, humidity, and stability is associated with marine warm-cloud microphysics,  
28 providing observational constraints for climate model representation of ACI.

29

30 **1 Introduction**

31 Aerosol–cloud interactions (ACI) play a crucial role in regulating Earth’s radiative balance and  
32 hydrological cycle by altering cloud microphysical and macrophysical properties (Bellouin et al., 2020;  
33 Jia et al., 2021; Rosenfeld et al., 2019; Stier et al., 2024; Wang et al., 2024c; Zhao et al., 2024). Numerous  
34 studies have demonstrated that ACI are strongly modulated by environmental conditions, such as lower-  
35 tropospheric stability (Chen et al., 2014; Wang et al., 2014), relative humidity (Douglas and L’Ecuyer,

36 2019), precipitable water vapor (Qiu et al., 2017; Yuan et al., 2008; Zheng et al., 2022), vertical velocity  
37 (Jia et al., 2022; Su et al., 2010), wind shear (Fan et al., 2009; Kim et al., 2003) , and the vertical overlap  
38 between aerosol and cloud layers (Costantino and Bréon, 2013). However, over the South China Sea  
39 (SCS), a region strongly influenced by pronounced monsoon circulation, the observational evidence of  
40 how ACI respond to variations in thermodynamic and moisture conditions remains limited.

41 The SCS, one of the world’s largest marginal seas, provides a unique natural laboratory for investigating  
42 ACI under the alternating influence of two opposing monsoon systems. The SCS experiences a  
43 pronounced seasonal reversal of wind regimes, characterized by a warm, moist southwest monsoon  
44 during boreal summer and a cool, dry northeast monsoon during boreal winter (Wang et al., 2009).  
45 During the southwest monsoon period, the marine boundary layer over the northern SCS becomes  
46 unstable, with enhanced air–sea temperature differences and surface turbulent heat fluxes that intensify  
47 vertical mixing and deepen the boundary layer while reducing wind shear (Peng et al., 2016). Rainfall  
48 during this period is primarily governed by warm-cloud microphysical processes and vapor convergence-  
49 driven condensation (Wang et al., 2007). In contrast, during the northeast monsoon period, cold surges  
50 associated with the East Asian winter monsoon substantially modify the SCS boundary-layer structure  
51 by enhancing surface turbulent fluxes, deepening the mixed layer, and strengthening the inversion that  
52 promotes extensive low-cloud development (Wang et al., 2024a). The SCS is also a region that is  
53 simultaneously affected by various types of aerosols from industrial emissions, shipping activities, and  
54 biomass burning. It has been shown that those aerosols substantially modify the microphysical structure  
55 of marine boundary layer clouds over the SCS by increasing small droplet concentrations and suppressing  
56 midsize droplets near cloud base (Miller et al., 2023). Recent shipborne observations further reveal that  
57 aerosol sources over the SCS exhibit distinct seasonal contrasts, being dominated by continental outflow  
58 from mainland Southeast Asia during the southwest monsoon and by pollution plumes transported from  
59 continental China during the northeast monsoon (Ou et al., 2025). Yet, how these contrasting aerosol and  
60 meteorological regimes modulate ACI, particularly for warm non-raining clouds, remains poorly  
61 quantified.

62 Quantifying ACI is essential for constraining their climatic impacts. According to the Sixth Assessment  
63 Report of the Intergovernmental Panel on Climate Change (Douville et al., 2023) , the effective radiative

64 forcing associated with ACI ( $ERF_{aci}$ ) is estimated to be  $-0.84 \text{ W m}^{-2}$  globally, with a wide 5–95%  
65 confidence range from  $-1.45 \text{ W m}^{-2}$  to  $-0.25 \text{ W m}^{-2}$ , dominating the overall uncertainty in total aerosol  
66 effective radiative forcing, which ranges between  $-1.7$  and  $-0.4 \text{ W m}^{-2}$ .  $ERF_{aci}$  may be further  
67 decomposed into two components: the instantaneous radiative forcing due to ACI, also known as the  
68 Twomey effect ( $RF_{aci}$ , Twomey, 1977, 1974), and rapid adjustments (Ackerman et al., 2004; Albrecht,  
69 1989; Bellouin et al., 2020). To quantify the cloud response to aerosol perturbations, Feingold et al.  
70 (2001) proposed the ACI index ( $ACI_r$  and  $ACI_{Nd}$ ), which has since become a widely used metric for  
71 evaluating the strength of the Twomey effect in both satellite and in-situ studies, defined as:

$$72 \quad ACI_r = -d \ln r / d \ln \alpha \quad (1)$$

$$73 \quad ACI_{Nd} = d \ln N_d / d \ln \alpha \quad (2)$$

74 where  $r$  and  $N_d$  denote the cloud effective radius and droplet number concentration, respectively, and  $\alpha$   
75 is an aerosol proxy (e.g., AOD, AI, or NCCN). In this study, AI is employed as the aerosol proxy in the  
76 calculation of ACI.  $ACI_{Nd}$  is more recently also referred to as the Nd susceptibility to aerosols (Ma et al.,  
77 2018a, b).

78 Although many studies have examined the environmental modulation of ACI over both oceanic and  
79 continental regions (Fan et al., 2016; Jia et al., 2019, 2022; Jia and Quaas, 2023; Seinfeld et al., 2016;  
80 Sorooshian et al., 2019; Wall et al., 2022; Wang et al., 2024d), such processes remain poorly constrained  
81 over the SCS. The pronounced seasonal reversal of monsoon circulation in this region creates highly  
82 contrasting thermodynamic and moisture conditions, along with differing aerosol regimes, which  
83 together exert distinct influences on cloud microphysics and modulate the ACI processes. Therefore, this  
84 study aims to provide a comprehensive assessment of ACI in non-raining warm clouds over the SCS  
85 under different monsoon regimes. Long-term multi-satellite and reanalysis datasets from July 2002 to  
86 February 2020 are integrated to characterize variations in aerosol, cloud, and environmental properties  
87 across the southwest monsoon wet (SWMW), northeast monsoon wet (NEMW), and northeast monsoon  
88 dry (NEMD) phases, and to quantitatively evaluate the corresponding ACI responses. Particular attention  
89 is given to understanding how variations in water vapor availability and lower-tropospheric stability  
90 (LTS) influence the sensitivity of cloud microphysical responses to aerosol perturbations.

91 The paper is organized as follows. Section 2 describes the datasets and method used in this study. The  
 92 main findings and related discussions are presented in Section 3. Section 4 summarizes the key findings  
 93 and conclusions.

## 94 **2 Data and Methods**

95 This study employs long-term, multi-source datasets to investigate ACI over the SCS. The cloud  
 96 properties are derived from the Clouds and the Earth’s Radiant Energy System (CERES)–Moderate  
 97 Resolution Imaging Spectroradiometer (MODIS) Edition 4 Level-3 product (SSF1deg, Aqua, daytime).  
 98 Cloud droplet number concentration (Nd) data are obtained from a community-standard gridded dataset  
 99 provided by Gryspeerdt et al. (2022). Aerosol optical properties is obtained from the Modern-Era  
 100 Retrospective analysis for Research and Applications, Version 2 (MERRA-2). Meteorological fields are  
 101 taken from the European Centre for Medium-Range Weather Forecasts (ECMWF) fifth-generation  
 102 reanalysis (ERA5). Precipitation data are provided by the Integrated Multi-satellite Retrievals for GPM  
 103 (IMERG) Version 7 Final Run, and sea surface temperature (SST) data are obtained from the National  
 104 Oceanic and Atmospheric Administration (NOAA) Optimum Interpolation (OI) SST, version 2. The  
 105 definitions of the monsoon regimes and the analyses of large-scale circulation, aerosol, and cloud  
 106 properties are conducted at their native spatial resolutions. For aerosol–cloud collocation, AOD, AI, and  
 107 ERA5 meteorological fields used in the calculation of ACI and environmental stratification are regridded  
 108 to a common  $1^\circ \times 1^\circ$  grid using bilinear interpolation with the Climate Data Operators (CDO, remapbil).

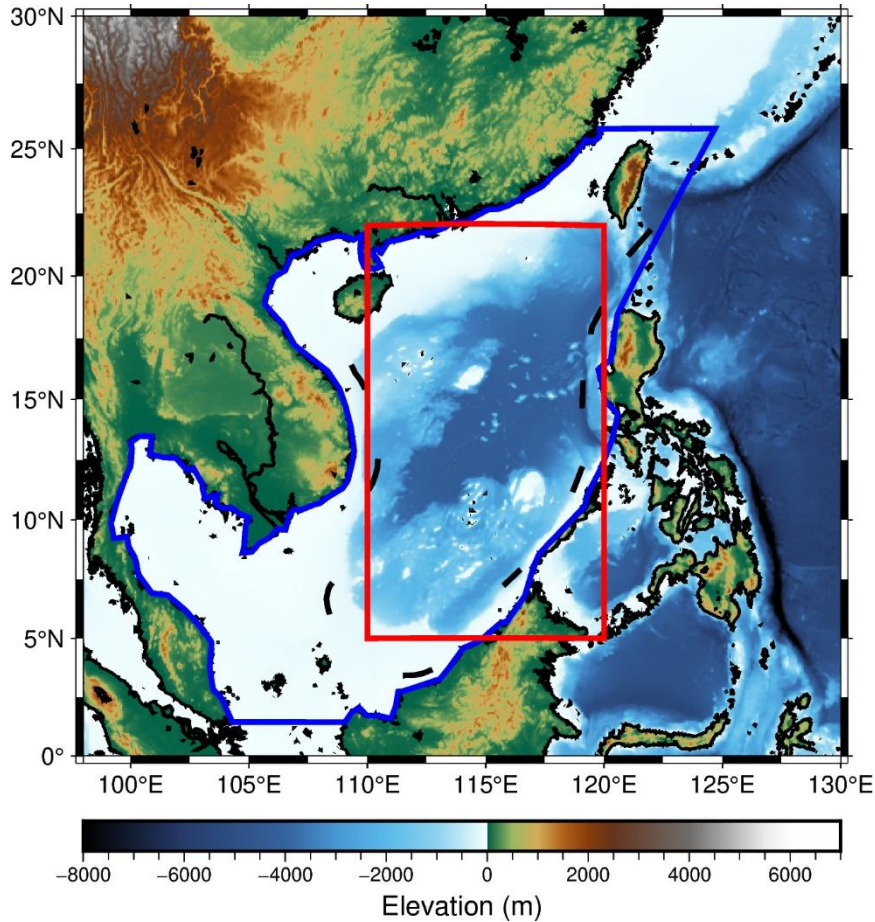
109 **Table 1: Overview of datasets used in this study.**

Parameter	Data Source	Spatial Resolution	Temporal Resolution	Data Range
Cloud Effective Radius	CERES–MODIS V04 (Aqua, daytime)	$1^\circ \times 1^\circ$	daily	Jul 2002 –
Cloud Optical Thickness				Feb 2020
Cloud-top Temperature				
Cloud-top Pressure				
Liquid Cloud Area Fraction				
Liquid Water Path				
Cloud Droplet Number Concentration	Gryspeerdt et al. (2022)	$1^\circ \times 1^\circ$	daily	Jul 2002 – Feb 2020
Total Aerosol Extinction (550 nm)	MERRA-2	$0.5^\circ \times 0.625^\circ$	daily	Jul 2002 – Feb 2020

Total Parameter (470–870 nm)	Aerosol Ångström					
Specific Humidity	ERA5	0.25°	×	daily	Jul 2002 –	
Temperature		0.25°			Feb 2020	
Relative Humidity						
Horizontal Wind Components						
Mean Sea Level Pressure						
Precipitation	IMERG V07 Final	0.1° × 0.1°		30 min	Jul 2002 – Feb 2020	
Sea Surface Temperature	NOAA OI SST V2	1° × 1°		monthly	Jul 2002 – Feb 2020	

## 110 2.1 Study Area

111 SCS is one of the world’s largest marginal seas, characterized by complex air–sea interactions and a  
112 pronounced seasonal reversal of wind systems (Wang et al., 2009). This region is strongly influenced by  
113 the Asian monsoon circulation, exhibiting distinct southwest and northeast monsoon regimes that  
114 profoundly modulate its thermodynamic and dynamic environments (Zheng et al., 2025). These  
115 alternating monsoon circulations govern the regional aerosol loading (Ou et al., 2025), boundary-layer  
116 structure (Chen et al., 2025; Peng et al., 2016; Wang et al., 2024a), and cloud microphysical processes  
117 (Miller et al., 2023; Wang et al., 2024b), making the SCS an ideal natural laboratory for investigating  
118 ACI under contrasting meteorological conditions. In this study, the analysis domain (blue polygon in  
119 Fig. 1) encompasses the entire SCS, including both coastal and open-ocean areas, to capture the spatial  
120 variability of aerosol, cloud, and environmental parameters. The red box in Fig. 1 delineates the  
121 subregion (3°–22° N, 110°–120° E) used for defining the monsoon regimes following Wang et al. (2004).



122

123 **Figure 1: Study region and monsoon classification over the South China Sea. The blue polygon indicates the**  
 124 **study domain, while the red box marks the region used for defining the monsoon regimes.**

125 **2.2 Cloud Remote Sensing Products**

126 Cloud retrievals used in this study are derived from the Moderate Resolution Imaging Spectroradiometer  
 127 (MODIS) aboard the Aqua satellite, which has an equatorial crossing time of approximately 1:30 p.m.  
 128 local time. The MODIS cloud products analysed are obtained from the Clouds and the Earth’s Radiant  
 129 Energy System (CERES) MODIS (CERES–MODIS hereafter) Edition 4 (Minnis et al., 2011a, 2021)  
 130 Single Scanner Footprint (SSF) daily products (Level 3,  $1^\circ \times 1^\circ$  grid resolution), which provide  
 131 physically consistent cloud and radiative properties based on synergistic MODIS and CERES  
 132 observations. The CERES–MODIS cloud retrievals have been extensively validated (Minnis et al.,  
 133 2011b; Yost et al., 2021) and have been widely employed in studies of ACI (Jia et al., 2021; Painemal,  
 134 2018). CERES–MODIS Edition 4 SSF cloud parameters utilized here include cloud optical depth ( $\tau$ ),  
 135 cloud effective radius (CER), cloud-top temperature (CTT), cloud-top pressure (CTP), liquid cloud area

136 fraction (LCAF), and liquid water path (LWP). CER is retrieved from the 3.7- $\mu\text{m}$  channel, which is less  
137 affected by retrieval biases than its 2.1- and 1.6- $\mu\text{m}$  counterparts (Grosvenor et al., 2018).  
138  $N_d$  used in this study is obtained from the community-standard gridded dataset of Gryspeerdt et al.  
139 (2022), which provides  $1^\circ \times 1^\circ$  Level-3  $N_d$  products derived from pixel-level MODIS Collection 6.1  
140 retrievals. In this dataset,  $N_d$  is first estimated at the native MODIS pixel scale using retrieved cloud  
141 optical thickness and cloud effective radius, and then aggregated to a common grid using established  
142 sampling strategies to ensure robustness and consistency. The  $N_d$  retrievals are based on the adiabatic  
143 cloud assumption and are subject to strict quality control procedures, including screening for optically  
144 thin clouds, large solar zenith angle and viewing zenith angle conditions, sub-pixel heterogeneity, and  
145 potential retrieval contamination. Only single-layer liquid cloud scenes are retained. This dataset has  
146 been evaluated against observations and is widely used in aerosol–cloud interaction studies (e.g., Jia et  
147 al., 2024; Wall et al., 2023). In this study, we use the  $N_{d\_G18\_37}$  product from this community-standard  
148 dataset.

### 149 **2.3 Aerosol Optical Properties**

150 Aerosol properties used in this study are obtained from the Modern-Era Retrospective Analysis for  
151 Research and Applications, Version 2 (MERRA-2, Gelaro et al., 2017), which assimilates a wide range  
152 of satellite observations to provide a physically consistent representation of global aerosol distributions.  
153 The MERRA-2 aerosol dataset used here includes the total aerosol extinction (AOD, 550 nm) and the  
154 total aerosol Ångström parameter (AE, 470-870 nm), with a spatial resolution of  $0.5^\circ \times 0.625^\circ$  and a  
155 temporal resolution of 1 hour. To ensure spatiotemporal consistency with the CERES–MODIS cloud  
156 products, the MERRA-2 aerosol fields at 14:00 local solar time (LST), closest to the Aqua overpass  
157 (~13:30 LST), were regridded to a  $1^\circ \times 1^\circ$  grid. AOD represents the column-integrated aerosol extinction,  
158 whereas AE characterizes the wavelength dependence of AOD and is commonly used as an indicator of  
159 aerosol particle size. A higher AE generally indicates dominance of fine-mode aerosols, while a lower  
160 AE suggests coarse-mode particles. The aerosol index (AI) is defined as the product of AOD and AE:

$$161 \quad \text{AI} = \text{AOD} \times \text{AE} \quad (3)$$

162 AI, in comparison to AOD, is considered a better parameter for representing aerosols in ACI studies,  
163 because it incorporates information on aerosol particle size, which is critical for cloud droplet activation

164 and microphysical properties (Ma et al., 2018b; Nakajima et al., 2001). Therefore, AI is employed in this  
165 study as the aerosol proxy in the calculation of ACI.

#### 166 **2.4 Atmospheric Parameters of Weather Fields**

167 Atmospheric fields were obtained from the fifth-generation ECMWF reanalysis (ERA5, Hersbach et al.,  
168 2020). ERA5 assimilates a comprehensive suite of ground-based and satellite observations through a  
169 state-of-the-art four-dimensional variational data assimilation system, offering physically consistent and  
170 dynamically balanced representations of the atmosphere. The dataset used here includes three-  
171 dimensional fields of specific humidity and horizontal wind components (U and V) at all standard  
172 pressure levels, temperature at 1000 and 700 hPa, and mean sea level pressure. The daily mean specific  
173 humidity and wind speed at 850 hPa were used to distinguish the three periods over the SCS (Wang et  
174 al., 2004). Wind and humidity fields at all pressure levels were analysed to characterize the large-scale  
175 atmospheric circulation and vertical moisture structure during these periods. The 1000 hPa specific  
176 humidity was employed as a proxy for the ambient water vapor available to warm clouds (Dadashazar et  
177 al., 2020). Temperatures at 1000 and 700 hPa were used to compute the LTS, which quantifies the  
178 thermodynamic stability of the lower atmosphere (Klein and Hartmann, 1993), as follows:

179

$$180 \quad LTS = \theta_{700hPa} - \theta_{1000hPa}$$
$$\theta = T \left( \frac{P_{00}}{P} \right)^{\frac{R}{C_p}} \quad (4)$$

181 where  $\theta_{700}$  and  $\theta_{1000}$  denote the potential temperatures at 700 and 1000 hPa, respectively,  $P_{00}$  is the  
182 standard reference pressure (typically 1000 hPa),  $P$  is the pressure at a given level,  $R$  is the gas constant  
183 for dry air, and  $C_p$  is the specific heat capacity of dry air at constant pressure. To ensure spatiotemporal  
184 consistency with the aerosol and cloud parameters, both the 1000 hPa specific humidity and LTS at 14:00  
185 LST were regridded to a  $1^\circ \times 1^\circ$  grid. Sea surface temperature (SST) was obtained from the National  
186 Oceanic and Atmospheric Administration (NOAA) Optimum Interpolation SST, version 2 (OI SST v2,  
187 Reynolds et al., 2002), which incorporates both in-situ and satellite observations and provides monthly  
188 fields at  $1^\circ \times 1^\circ$  resolution.

## 189 **2.5 Precipitation Data**

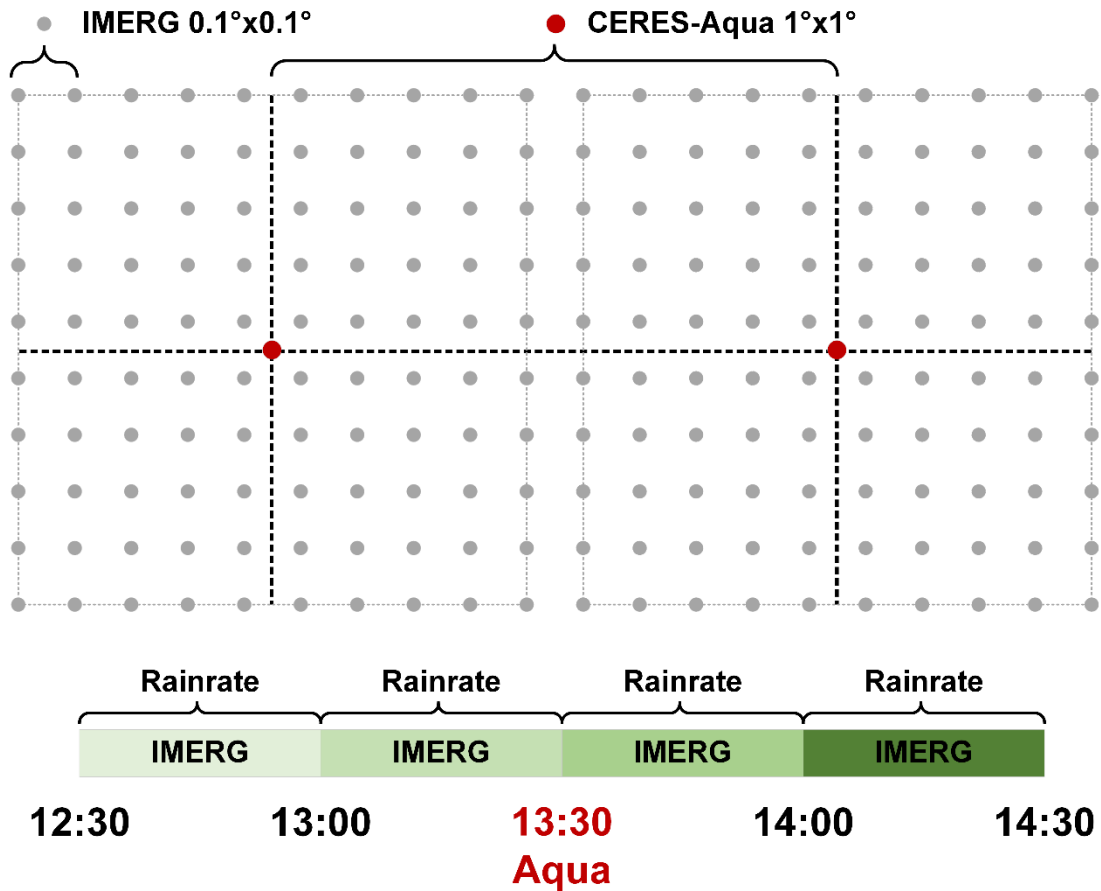
190 Precipitation data were obtained from the Integrated Multi-satellite Retrievals for GPM (IMERG)  
191 Version 07 Final run. IMERG is the flagship precipitation product of the Global Precipitation  
192 Measurement (GPM) mission, a collaborative effort between NASA and JAXA (Huffman et al., 2023).  
193 The IMERG algorithm calibrates, merges, and interpolates precipitation estimates from the constellation  
194 of Low Earth Orbit (LEO) passive microwave (PMW) radiometers onboard GPM satellites. These  
195 estimates are subsequently integrated with geostationary satellite infrared observations, particularly in  
196 regions with sparse PMW coverage, to produce a global precipitation product with  $0.1^\circ$  spatial and 30-  
197 minute temporal resolutions (Huffman et al., 2020; Watters et al., 2021). IMERG precipitation data,  
198 owing to its global coverage and high spatiotemporal resolution, have been widely adopted by the  
199 research community (Dezfuli et al., 2017; Durden, 2024; Hayden et al., 2023; Tan et al., 2019a; Watters  
200 et al., 2021; Watters and Battaglia, 2019; Zhang and Wang, 2024; Zhu et al., 2024). Consequently,  
201 IMERG V07 Final Run PrecipitationCal, the gauge-calibrated multi-satellite product, is used here to  
202 determine whether precipitation occurred within each CERES–MODIS grid cell.

## 203 **2.6 Data Quality Control**

204 To minimize the influence of satellite retrieval biases when investigating ACI, a rigorous quality-control  
205 procedure was applied to the CERES–MODIS cloud dataset following the method of Saponaro et al.  
206 (2017). The selection criteria were as follows:

- 207 1. Only liquid-phase warm clouds were retained, identified by a cloud-phase flag of “liquid” and CTT  
208  $> 273$  K.
- 209 2. To reduce the impact of large-scale cloud-macrophysical variability and highlight microphysical  
210 processes, only clouds with CTP between 650 and 950 hPa were selected.
- 211 3. Thin clouds with  $\tau < 5$  were excluded to minimize retrieval uncertainty.
- 212 4. A threshold of  $< 0.2$  mm  $\text{h}^{-1}$  was adopted to identify IMERG non-raining cases, following Tan et al.  
213 (2019b). The IMERG precipitation data were first collocated onto CERES–MODIS  $1^\circ \times 1^\circ$  grid  
214 cells. A grid cell was then classified as non-raining when all IMERG sub-pixels within the 13:00–

215 13:30 and 13:30–14:00 local time intervals recorded precipitation rates below  $0.2 \text{ mm h}^{-1}$ , as  
 216 illustrated in Fig. 2.



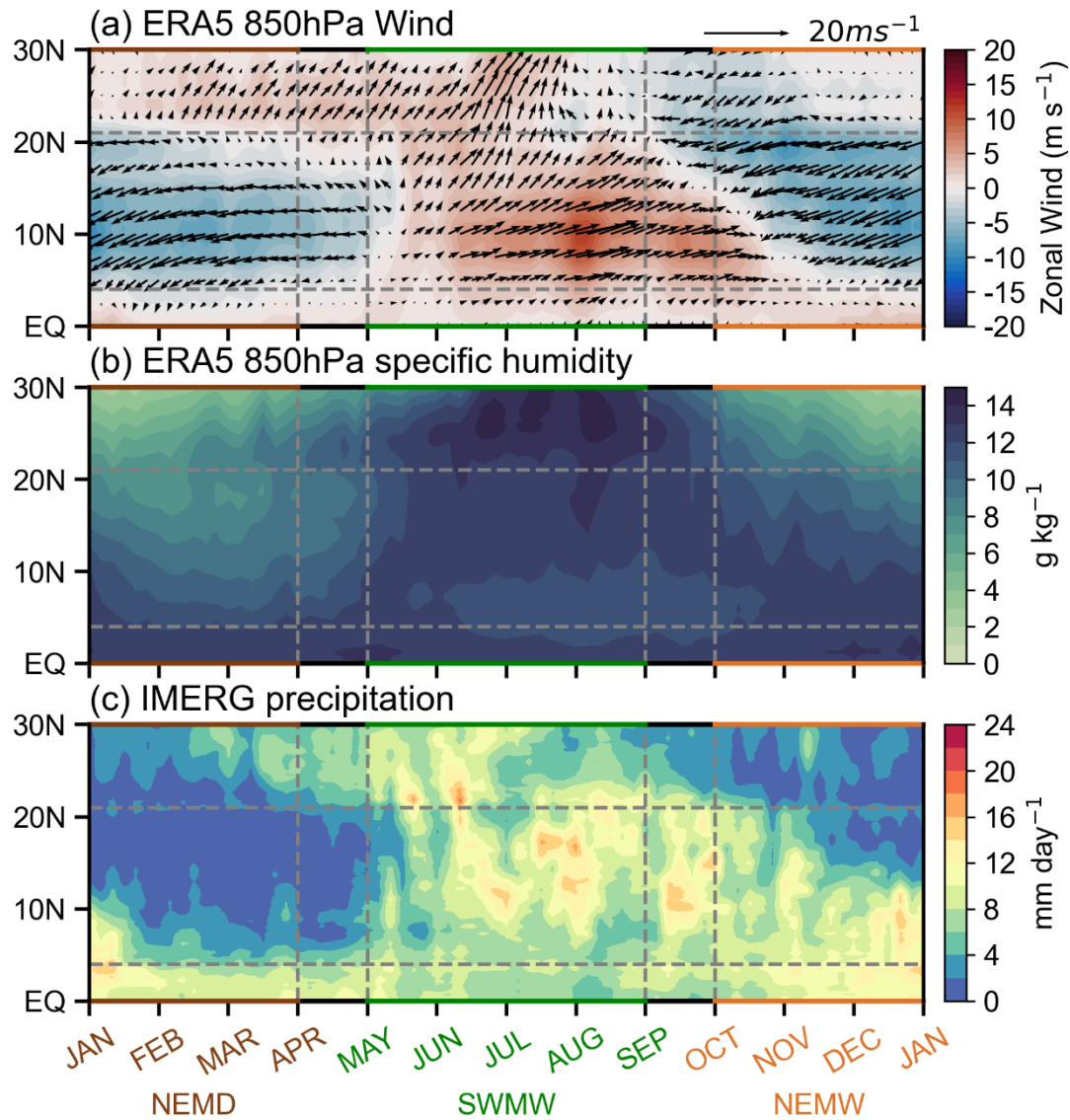
217  
 218 **Figure 2: Schematic illustration of the procedure used to identify non-raining CERES–MODIS grid cells**  
 219 **based on IMERG V07 Final Run PrecipitationCal.**

220 **3 Result**

221 **3.1 Definition of Monsoon Periods over the South China Sea**

222 ACI are strongly modulated by environmental factors such as humidity, vertical wind velocity, and  
 223 atmospheric stability (Zhu et al., 2022). Therefore, considering the prevailing atmospheric conditions is  
 224 crucial when examining their variability. The atmospheric environment over the SCS exhibits distinct  
 225 characteristics under the influence of the southwest monsoon and the northeast monsoon. A distinctive  
 226 feature of the SCS summer monsoon is its nearly simultaneous onset across a broad latitudinal range  
 227 ( $3^{\circ}$ – $22^{\circ}$ N) (Wang et al., 2004). On top of the previous studies that defined monsoon periods over the  
 228 SCS based on wind direction (Wang et al., 2004, 2009), we further incorporated precipitation and specific  
 229 humidity within this  $3$ – $22^{\circ}$ N band (the red box in Fig. 1) to classify the study periods into three regimes:

230 the southwest monsoon wet period (SWMW), the northeast monsoon dry period (NEMD), and the  
231 northeast monsoon wet period (NEMW). As shown in Fig. 3, the SCS is dominated by the southwest  
232 monsoon from May to August, during which specific humidity reaches its maximum and precipitation is  
233 strongest. From October to December, the northeast monsoon prevails, accompanied by relatively high  
234 specific humidity and intense precipitation. During January to March, the SCS remains under the  
235 influence of the northeast monsoon, but specific humidity is at its lowest and precipitation is minimal,  
236 representing a dry period. Accordingly, we defined May–August as SWMW, October–December as  
237 NEMW, and January–March as NEMD. These three periods not only reflect significant differences in  
238 atmospheric circulation and moisture conditions, along with aerosol regimes over the SCS, but also  
239 provide distinct environmental backgrounds for ACI, which may influence their characteristics and  
240 intensity.



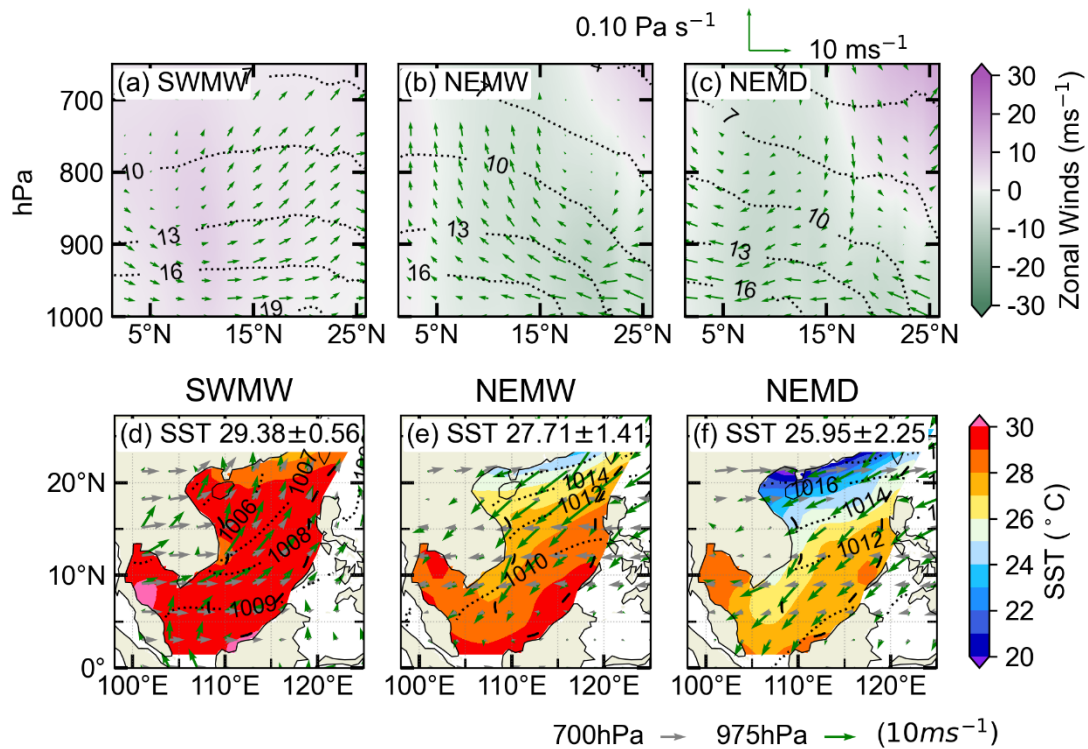
241  
 242 **Figure 3:** Time–latitude distribution of the (a) ERA5 climatological pentad mean 850 hPa zonal wind (Jul  
 243 2002–Feb 2020) and (b) ERA5 pentad mean 850 hPa specific humidity (Jul 2002–Feb 2020) and (c) IMERG  
 244 pentad mean precipitation (Jul 2002–Feb 2020). The data are averaged over the longitude bands between  
 245 110E and 120E across the SCS. The arrows in (a) indicates 850hPa horizontal winds.

## 246 3.2 Atmospheric conditions and Aerosol–Cloud properties during the Three Periods

### 247 3.2.1 Atmospheric Circulation and Sea Surface Temperature

248 The Hadley circulation over the SCS is modulated by the Asian monsoon system and the seasonal  
 249 variation of solar radiation. Fig. 4a shows that during the SWMW period, the SCS is dominated by  
 250 ascending motion, which is associated with the presence of the Intertropical Convergence Zone (ITCZ)  
 251 over the region. During the NEMW period, the Hadley circulation shifts southward and the subtropical  
 252 high is established over the northern SCS (Fig. 4e). As a result, subsidence dominates the northern part

253 of the region, whereas ascending motion occurs over the equatorial southern part (Fig. 4b). During the  
 254 NEMD period, as the Hadley circulation continues to shift southward, the subtropical high dominates  
 255 the SCS (Fig. 4f), leading to prevailing subsidence over the region (Fig. 4c). As shown in Figs. 4a-c, the  
 256 water vapor content over the SCS gradually decreases from the SWMW period to the NEMW period and  
 257 further to the NEMD period. During the SWMW period, the winds over the SCS are predominantly  
 258 westerly. In contrast, during both the NEMW and NEMD periods, the winds are mainly easterly.  
 259 Additionally, a westerly jet is present at upper levels over the northern SCS. These features show that  
 260 the SCS exhibits distinct vertical circulation, moisture, and wind patterns under different monsoon  
 261 conditions.



262  
 263 **Fig. 4.** Zonally averaged cross section of the atmospheric circulation from ERA5 (Jul 2002–Feb 2020) for the  
 264 domain bounded between 110°E and 120°E during (a) the southwest monsoon wet period, (b) the northeast  
 265 monsoon wet period, and (c) the northeast monsoon dry period. Meridional and pressure velocity are denoted  
 266 by arrows ( $\uparrow$  indicates upward motion), whereas colors indicate the zonal wind component. Black contour is  
 267 specific humidity. Panels (d–f) show the corresponding overview of meteorological conditions and SST over  
 268 the SCS region. Color shades represent SST from OISST (Jul 2002–Feb 2020), black contour is sea level  
 269 pressure from ERA5 (Jul 2002–Feb 2020), and arrows are near-surface wind speed at 975 hPa (green) and  
 270 that at 700 hPa (gray) from ERA5 (Jul 2002–Feb 2020).

271 The SCS exhibits contrasting large-scale circulation patterns between the southwest and northeast  
 272 monsoon periods, as shown in Figs. 4d–f. During the SWMW period, the SCS is influenced by tropical

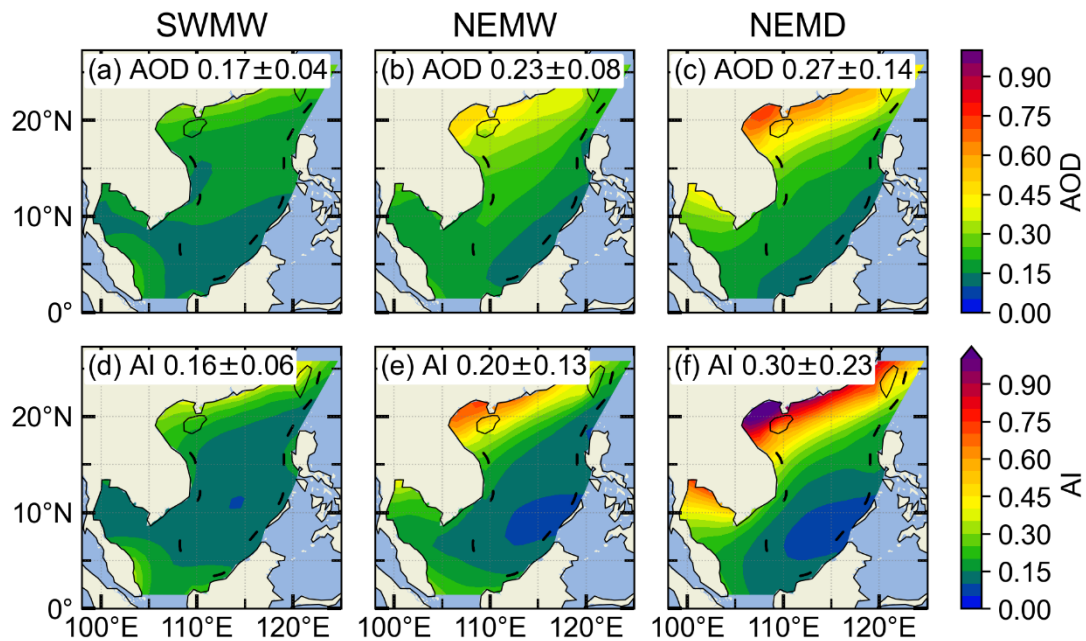
273 and equatorial maritime air masses, with prevailing southwesterlies over the region (Martin and  
274 Howland, 1982), whereas during the northeast monsoon, winter airflows originating from Siberia and  
275 the Mongolian Plateau result in prevailing northeasterlies (Liu et al., 2024). These opposite prevailing  
276 wind directions play a crucial role in modulating the transport pathways of continental pollutants into the  
277 SCS. Specifically, air masses originating from the Indochinese Peninsula and surrounding Southeast  
278 Asian land regions are the primary sources of pollutants transported into the SCS (Miller et al., 2023; Ou  
279 et al., 2025; Sun et al., 2023; Zhang et al., 2019), whereas during the northeast monsoon, continental  
280 emissions from China may be carried southward into the region (Xiao et al., 2017; Yuan et al., 2024;  
281 Zheng et al., 2023).

282 Figures 4d–f show that the area-averaged SST over the SCS is highest during the SWMW period ( $29.38$   
283  $\pm 0.56$  °C), lower during the NEMW period ( $27.71 \pm 1.41$  °C), and lowest during the NEMD period  
284 ( $25.95 \pm 2.25$  °C), with variations consistent with those of specific humidity. During the southwest  
285 monsoon, the SST gradient across the SCS is relatively small, whereas during the northeast monsoon,  
286 SST decreases with increasing latitude (Wu et al., 2020), and a cold water band forms along the coastal  
287 region near mainland China (Chen and Hu, 2023). Higher SST promotes strong latent and sensible heat  
288 fluxes, which in turn enhance the atmospheric moisture content over the region (Lee and Park, 2022;  
289 Zhang et al., 1995). Consequently, SST and atmospheric moisture exhibit consistent variations across  
290 the three periods. In addition, during the northeast monsoon, both the SST (Figs. 4e–f) and atmospheric  
291 moisture (Figs. 4b–c) decrease with increasing latitude, showing similar latitudinal gradients.

### 292 **3.2.2 Aerosol and cloud properties**

293 The area-averaged aerosol values over the SCS exhibit clear differences among the three periods (Fig.  
294 5). The lowest values occur during the SWMW period, with  $\text{AOD} = 0.17 \pm 0.04$  and  $\text{AI} = 0.16 \pm 0.06$ .  
295 Higher values are observed during the NEMW period, with  $\text{AOD} = 0.23 \pm 0.08$  and  $\text{AI} = 0.20 \pm 0.13$ ,  
296 whereas the NEMD period shows the highest values, with  $\text{AOD} = 0.27 \pm 0.14$  and  $\text{AI} = 0.30 \pm 0.23$ ,  
297 indicating different aerosol sources. Significant differences in aerosol distribution are also observed  
298 between the southwest and northeast periods. During the southwest period, higher aerosol values are  
299 found in the northern SCS near mainland China and in the southwestern SCS near Malaysia. During the  
300 northeast period, aerosol values exhibit a pronounced gradient, forming a coastal band that decreases

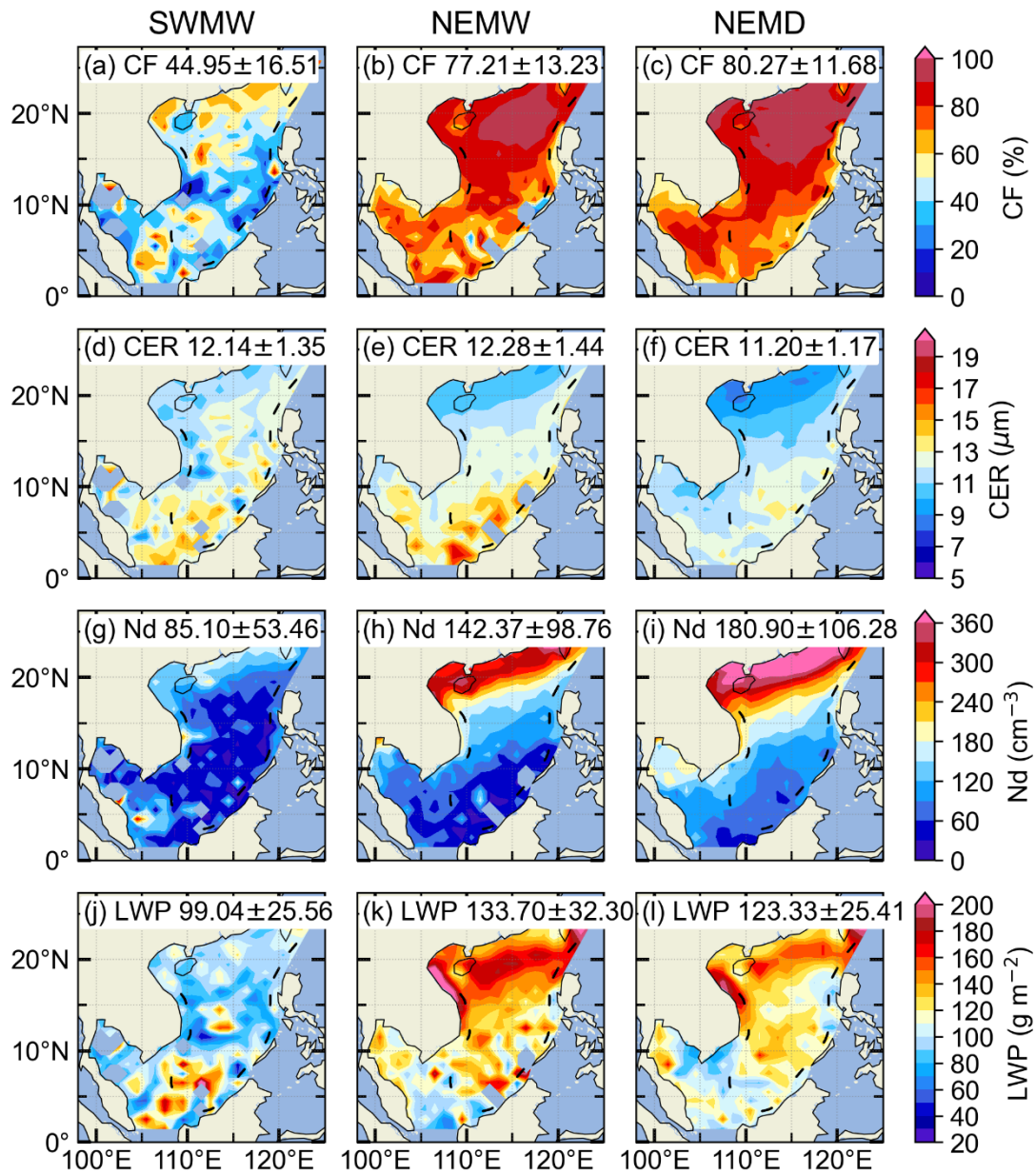
301 with increasing distance from the shoreline (Tu et al., 2021). Compared with AOD, AI incorporates  
 302 aerosol size information and is therefore considered a more suitable proxy for cloud condensation nuclei  
 303 in studies of ACI (Nakajima et al., 2001). Over the northern SCS near mainland China, AI values are  
 304 larger than AOD, indicating that aerosols in this region are dominated by fine particles. In contrast, in  
 305 the central SCS, farther from the continent, AI values are smaller than AOD, suggesting that aerosols  
 306 there are primarily coarse particles from natural sources.



307  
 308 **Figure 5: Spatial distributions of MERRA-2 AOD (Jul 2002–Feb 2020) over the South China Sea, averaged**  
 309 **over different periods: (a) the southwest monsoon wet period, (b) the northeast monsoon wet period, and (c)**  
 310 **the northeast monsoon dry period. (d–f) Corresponding AI (Jul 2002–Feb 2020) averaged over the same**  
 311 **periods.**

312 Figure 6 shows the variations in macrophysical and microphysical properties of warm clouds over the  
 313 SCS during the three monsoon periods. During the SWMW period, the area-averaged warm-cloud  
 314 fraction over the SCS is the lowest ( $44.95 \pm 16.51$  %), whereas comparable higher values are observed  
 315 during the NEMW ( $77.21 \pm 13.23$  %) and NEMD ( $80.27 \pm 11.68$  %) periods. Although the SCS  
 316 experiences the highest water vapor content during the SWMW period, the presence of strong updrafts  
 317 enhances cloud development (Fig. 4a), leading to the lowest fraction of warm clouds and an increased  
 318 occurrence of mixed-phase and ice clouds. During the northeast monsoon, the advection of dry and cold  
 319 continental air over the SCS likely suppresses convective activity, maintaining a higher fraction of warm  
 320 clouds in the region. Additionally, During the northeast monsoon, the fraction of warm clouds is highest

321 in the northern SCS, whereas lower values are observed in the southern region near the equator, likely  
 322 due to stronger convective activity in the equatorial area.



323  
 324 **Figure 6: Spatial distributions of warm-cloud (a–c) cloud fraction, (d–f) cloud droplet effective radius, (g–i)**  
 325 **cloud droplet number concentration, and (j–l) liquid water path over the South China Sea during the**  
 326 **southwest monsoon (first column), the northeast monsoon wet period (second column), and the northeast**  
 327 **monsoon dry period (third column).**

328 The area-averaged warm-cloud droplet effective radius over the SCS is similar across the three monsoon  
 329 periods, with values of  $12.14 \pm 1.35 \mu\text{m}$  during the SWMW period,  $12.28 \pm 1.54 \mu\text{m}$  during the NEMW  
 330 period, and  $11.20 \pm 1.17 \mu\text{m}$  during the NEMD period (Figs. 6d–f). In terms of the spatial distribution of  
 331 warm-cloud droplet effective radius, droplets near the equatorial region tend to be larger than those in

332 other areas, likely due to more pronounced droplet collision and coalescence driven by precipitation,  
333 which increases droplet size.

334 The area-averaged warm-cloud droplet number concentration over the SCS exhibits distinct differences  
335 among the three periods. The lowest mean value occurs during the SWMW period ( $85.10 \pm 53.46 \text{ cm}^{-3}$ ),  
336 followed by a higher value during the NEMW period ( $142.37 \pm 98.76 \text{ cm}^{-3}$ ), and the highest value during  
337 the NEMD period ( $180.90 \pm 106.28 \text{ cm}^{-3}$ ) (Figs. 6g–i). The highest cloud droplet number concentration  
338 is observed in the northern SCS adjacent to the Chinese mainland, showing a strong spatial  
339 correspondence with aerosol distribution. Aerosol concentrations are also largest in this region (Fig. 5),  
340 consistent with the Twomey effect, whereby enhanced aerosol loading increases cloud droplet number  
341 concentration. In the southern SCS near the equator, cloud droplet number concentration is relatively  
342 low, which may be attributed to lower aerosol concentrations and/or stronger convective activity that  
343 promotes droplet growth and reduces droplet number.

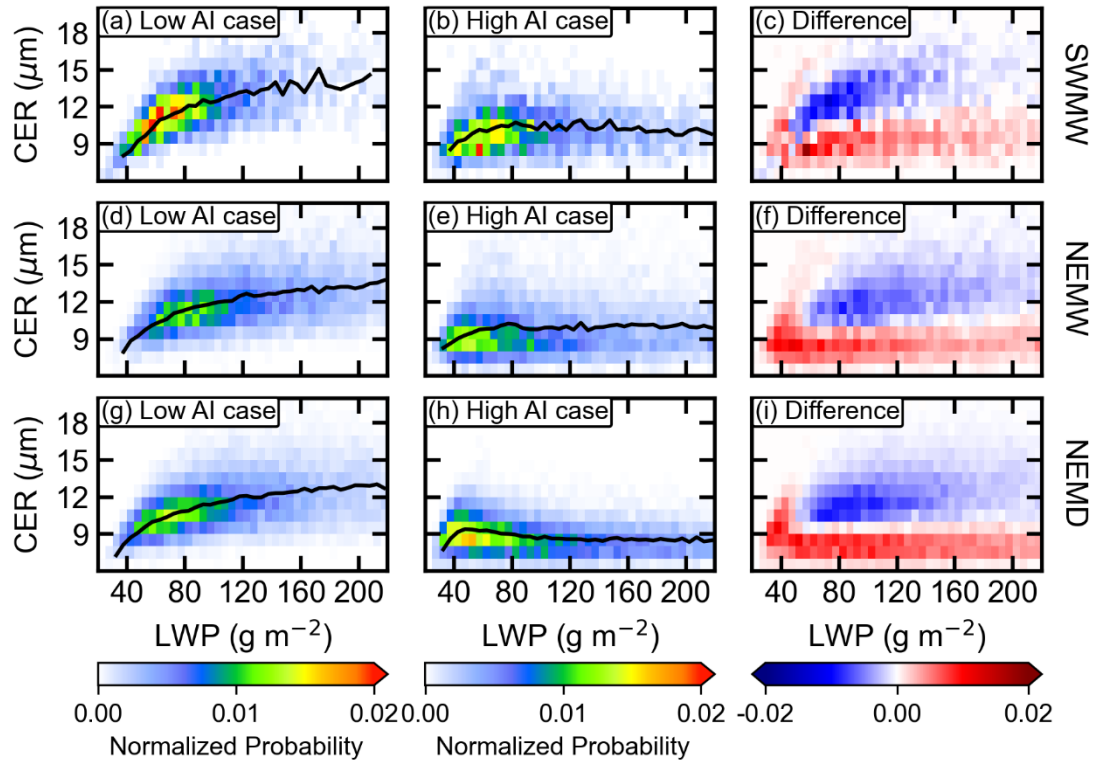
344 The area-averaged warm-cloud LWP over the SCS is lowest during the SWMW period ( $99.04 \pm 25.56 \text{ g}$   
345  $\text{m}^{-2}$ ), highest during the NEMW period ( $133.70 \pm 32.30 \text{ g m}^{-2}$ ), and intermediate during the NEMD period  
346 ( $123.21 \pm 25.41 \text{ g m}^{-2}$ ) (Figs. 6j–l). During the northeast monsoon, the highest LWP values are observed  
347 in the northern SCS adjacent to the Chinese mainland. This may be attributed to more polluted  
348 environments, where the second indirect aerosol effect suppresses precipitation, thereby leading to an  
349 increase in LWP (Albrecht, 1989). It is noteworthy that the LWP in the northern SCS is higher during  
350 the NEMW period than during the NEMD period, which may be associated with sedimentation-  
351 entrainment feedback (Ackerman et al., 2004) and/or evaporation-entrainment feedbacks (Dagan et al.,  
352 2017; Wang et al., 2003). Compared with the NEMW period, the NEMD period is characterized by  
353 higher cloud droplet number concentrations and smaller CER in this region (Fig. 6e, f, h, i). These two  
354 feedbacks describe how increased droplet number concentrations and reduced droplet sizes can enhance  
355 cloud-top entrainment and evaporation, ultimately leading to a reduction in LWP (Gryspeerd et al.,  
356 2019). Additionally, under drier conditions above cloud tops during the NEMD period, the  
357 sedimentation-entrainment feedback may be further amplified, resulting in a stronger reduction in LWP  
358 (Gryspeerd et al., 2019; Sato et al., 2018). During the SWMW, LWP is also relatively high in the  
359 southern SCS near the equator (Fig. 6j). In this region, CER is larger and  $N_d$  is lower (Figs. 6d, g), likely

360 due to stronger updrafts near the equator, which enhance the vertical development of warm clouds and  
361 result in higher cloud water content.

362 Qualitatively, the consistency in zonal gradients of aerosol and cloud properties across all three monsoon  
363 regimes clearly reflects the theoretical ACI signal: aerosols increase  $N_d$  while reducing droplet size,  
364 which in turn lowers precipitation probability and thereby increases LWP and CF. Quantitatively,  
365 however, ACI intensities vary depending on the meteorological background (to be discussed in detail in  
366 the following section).

### 367 **3.3 The Twomey Effect across the Three Periods**

368 Twomey (1977) proposed that atmospheric aerosol particles can act as cloud condensation nuclei, such  
369 that an increase in aerosol loading leads to a higher cloud droplet number concentration. Under a nearly  
370 constant liquid water content, this results in smaller cloud droplet effective radius. To examine the  
371 Twomey effect during the three periods, the 25th and 75th percentiles of the AI were used to define clean  
372 ( $AI < 25$ th percentile) and polluted ( $AI > 75$ th percentile) conditions, respectively. For each condition,  
373 two-dimensional probability density distributions were calculated as a function of CER and LWP. The  
374 difference in the two-dimensional probability densities between polluted and clean conditions therefore  
375 illustrates how CER varies with aerosol loading under quasi-constant LWP. As shown in Fig. 7, CER is  
376 mostly smaller than  $15 \mu\text{m}$ , justifying the effectiveness of the filtering of non-raining cases. Under clean  
377 conditions, the CER of warm cloud increases with LWP across all three periods. Under polluted  
378 conditions, however, CER initially increases with LWP and then tends to level off during the SW period  
379 and the NEMW period. During the NEMD period, CER exhibits an increase followed by a decrease with  
380 increasing LWP, and subsequently remains nearly constant. The difference plots between polluted and  
381 clean conditions clearly demonstrate that polluted samples are more concentrated toward smaller CER  
382 values compared with clean samples in each quasi-constant LWP bin. This consistent shift toward  
383 smaller droplet sizes under higher aerosol loading demonstrates a clear manifestation of the Twomey  
384 effect during all three periods.



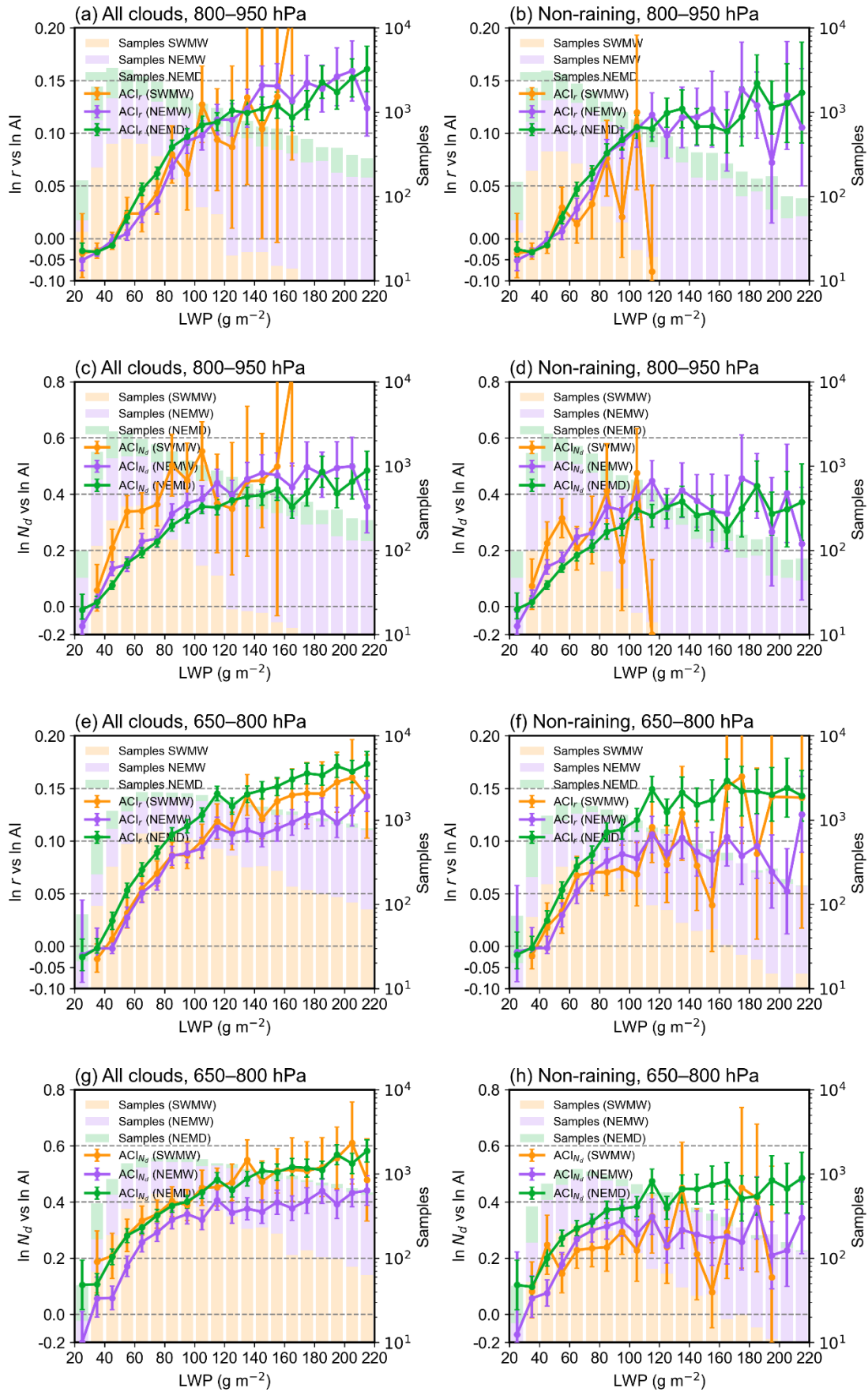
385

386 **Figure 7: Joint probability distributions of liquid water path (LWP) and cloud droplet effective radius (CER)**  
 387 **for warm clouds over the South China Sea during the three periods. The first, second, and third rows**  
 388 **correspond to the southwest monsoon, the northeast monsoon wet period, and the northeast monsoon dry**  
 389 **period, respectively. The first and second columns represent clean and polluted conditions, respectively. The**  
 390 **black lines denote the mean CER values within each LWP interval. The third column shows the differences**  
 391 **in probability density between polluted and clean conditions.**

### 392 3.4 Variations of ACI across the Three Periods

393 As shown in Fig. 6, the warm-cloud fraction during the Southwest Monsoon Wet period is approximately  
 394 45%, while it increases to about 77% during the Northeast Monsoon Wet period and further to about  
 395 80% during the Northeast Monsoon Dry period. This substantial difference suggests that the warm-cloud  
 396 populations sampled during different monsoon periods are fundamentally distinct and likely reflect  
 397 different cloud dynamical regimes. To better distinguish cloud morphological types within each monsoon  
 398 period and reduce potential regime-mixing effects, we further classified warm clouds over the SCS  
 399 according to CTP. Specifically, warm clouds were separated into shallow stratocumulus (CTP: 800–950  
 400 hPa) and deeper cumulus (CTP: 650–800 hPa) clouds. The ACI index were then quantified separately  
 401 for these two cloud regimes.

402 According to the assumption of the Twomey effect (Twomey, 1977), an essential prerequisite for  
403 investigating the aerosol indirect effect based on the CER–AI relationship is to keep the LWP constant.  
404 Since CER is a function of both LWP and AI, and generally increases with LWP, variations in LWP  
405 associated with changes in aerosols can in turn modulate the CER–AI relationship. Therefore, when  
406 applying the CER–AI relationship to analyse the first aerosol indirect effect, it is essential to constrain  
407 LWP to ensure its constancy. To satisfy this requirement while maintaining sufficient sample sizes, LWP  
408 was binned at  $10 \text{ g m}^{-2}$  intervals, within which  $\text{ACI}_r$  was examined separately for shallow stratocumulus  
409 (Fig. 8a-b) and deeper cumulus clouds (Fig. 8e-f) during the three periods. The results show that for both  
410 shallow stratocumulus and deeper cumulus clouds, under both all warm-cloud conditions and non-raining  
411 warm-cloud conditions,  $\text{ACI}_r$  is generally weak when  $\text{LWP} < 50 \text{ g m}^{-2}$ , and even exhibit the anti-Twomey  
412 effect (i.e., an increase in CER with increasing aerosol loading). Clouds in this LWP regime are typically  
413 very thin or broken, as well as post-precipitation remnants (McComiskey et al., 2009). A similar  
414 phenomenon is observed over the northern Indian Ocean, which may be attributed to the intense  
415 competition for available water vapor under high aerosol concentrations, combined with the entrainment  
416 of dry air at cloud tops (Jose et al., 2020). When  $\text{LWP} > 50 \text{ g m}^{-2}$ , the ACI for all cloud regimes across  
417 the three periods are consistent with the Twomey effect. An exception occurs in Fig. 8b and Fig. 8d,  
418 where the ACI at  $\text{LWP} = 120 \text{ g m}^{-2}$  during the southwest monsoon is negative. however, this result is not  
419 statistically robust due to the limited sample size.



421 **Figure 8: Linear regression slopes of  $\ln$  CER versus  $\ln$  AI and  $\ln$   $N_a$  versus  $\ln$  AI for shallow stratocumulus**  
422 **clouds (CTP = 800–950 hPa; a–d) and deeper cumulus clouds (CTP = 650–800 hPa; e–h) during the three**  
423 **periods. The first and second columns represent all cloud and non-raining cloud conditions, respectively.**  
424 **Green, purple, and yellow lines represent the southwest monsoon, northeast monsoon wet period, and**  
425 **northeast monsoon dry period, respectively. Error bars denote the 95 % confidence intervals of the linear**  
426 **regressions. Colored bars, consistent with the line colors, indicate the total number of samples within each**  
427 **LWP bin for the corresponding periods.**

428 Precipitation formation efficiently reduces cloud droplet number concentration and scavenges aerosols  
429 from clouds (Gryspeerd et al., 2015), introducing a sink of that does not reflect the Twomey effect (Jia et  
430 al., 2022). Therefore, when analyzing the aerosol first indirect effect in warm clouds, the influence of  
431 precipitation should be separated in order to accurately quantify the sensitivity of CER to aerosols. Fig.  
432 8 shows that, for both shallow stratocumulus and deeper cumulus clouds over the SCS, the  $ACI_r$  values  
433 for all warm cloud are consistently larger than those for non-raining warm-cloud across all three periods  
434 when LWP exceeds approximately  $80 \text{ g m}^{-2}$ . This indicates that the inclusion of raining samples amplifies  
435  $ACI_r$ , a phenomenon also identified in the AI/AOD– $N_a$  relationship by Jia et al. (2022) and Painemal et  
436 al. (2020). But this amplification is just an artifact governed by the joint impacts of the suppression of  
437 precipitation by aerosols and the aerosol removal by precipitation (Jia et al., 2022). Therefore, after  
438 removing precipitating clouds from all warm-cloud samples, the  $ACI_r$  obtained from non-raining warm  
439 clouds provides a more realistic representation. Nevertheless, the possibility of undetected light drizzle  
440 under high-LWP conditions may introduce additional uncertainty in the derived  $ACI$  estimates, despite  
441 precipitation screening using IMERG.

442 Fig. 8b. shows that, under non-raining warm-cloud conditions with  $LWP > 50 \text{ g m}^{-2}$ , the period-to-period  
443 variations in  $ACI_r$  differ between shallow stratocumulus and deeper cumulus clouds over the SCS. For  
444 shallow stratocumulus  $ACI_r$  values are broadly comparable across the three periods, with no significant  
445 differences (Fig. 8b). In contrast, deeper cumulus clouds exhibit clear differences among the three periods  
446 (Fig. 8f), with  $ACI_r$  generally strongest during the NEMD period, while the NEMW and SWMW periods  
447 show comparatively weaker values, with the NEMW period exceeding the SWMW period in some LWP  
448 bins. For  $LWP > 140 \text{ g m}^{-2}$ , the  $ACI_r$  during the southwest monsoon exhibits large fluctuations due to  
449 the limited number of samples, even exceeding that of the northeast monsoon. The analysis in Section  
450 3.2 reveals substantial differences in atmospheric conditions over the SCS among the three periods.

451 During the SWMW period, atmospheric moisture and sea surface temperatures reach their highest levels,  
452 and upward motion dominates over the region, while aerosol concentrations remain relatively low.  
453 During the NEMW period, moisture and sea surface temperatures are still relatively high, with upward  
454 motion primarily confined to the southern areas near the equator, and aerosol concentrations are elevated  
455 due to pollution transported from continental China. In contrast, during the NEMD period, atmospheric  
456 moisture and sea surface temperatures are at their lowest, subsidence dominates, and aerosol  
457 concentrations reach their maximum. These results suggest that although the large-scale environmental  
458 statistics differ substantially among the three monsoon periods, the local thermodynamic conditions  
459 favourable for shallow stratocumulus formation may be relatively similar across periods. Such cloud-  
460 favourable environments may not be fully resolved by the period-mean large-scale statistics presented  
461 here, which could explain the broadly comparable  $ACI_r$  values for shallow stratocumulus. In contrast,  
462  $ACI_r$  for deeper cumulus clouds over the SCS generally tends to strengthen under drier and more stable  
463 monsoon environments, with the strongest signals occurring during the NEMD period, while no  
464 consistent ordering is observed between the NEMW and SWMW periods across different LWP bins.  
465 Accordingly, the subsequent analysis focuses on the period-to-period differences of deeper cumulus  
466 clouds  $ACI$  and its relationship with variations in the monsoon environmental background.

467 In addition to the radius-based  $ACI_r$ , we further examined the droplet-number susceptibility ( $ACI_{Nd}$ )  
468 separately for shallow stratocumulus (Fig. 8c–d) and deeper cumulus clouds (Fig. 8g–h). Consistent with  
469 the  $ACI_r$  results,  $ACI_{Nd}$  for shallow stratocumulus remains broadly comparable across the three monsoon  
470 periods, with no significant differences. Deeper cumulus clouds exhibit clear period-to-period variations,  
471 with the strongest signals occurring during the NEMD period, while comparatively weaker values are  
472 observed during the SWMW and NEMW periods. The consistency between  $ACI_r$  and  $ACI_{Nd}$  suggests  
473 that the inferred  $ACI$  variations are robust to the choice of metric. However, because the two metrics are  
474 not independent, their agreement should be interpreted primarily as a consistency check rather than as  
475 independent evidence for the underlying physical mechanisms. Nevertheless, the similar inter-period  
476 variations exhibited by both metrics motivate a further examination of the environmental factors  
477 associated with these  $ACI$  differences. Therefore, Section 3.5 explores the potential influences of  
478 moisture and LTS on deeper cumulus cloud  $ACI$  across the three periods.

### 479 3.5 Causes of ACI Variations across the Three Periods

480 The progressive enhancement of  $ACI_r$  and  $ACI_{Nd}$  for deeper cumulus clouds from the SWMW to the  
481 NEMD period (Fig. 8) may potentially be influenced by the aerosol hygroscopic swelling artifact. The  
482 MERRA-2 AOD used to construct AI is calculated under ambient RH, with the extinction coefficients  
483 of sulfate, hydrophilic carbonaceous aerosols, and sea salt explicitly parameterized as functions of RH  
484 (Randles et al., 2017). Under humid conditions, aerosol hygroscopic growth can increase AOD, and  
485 therefore AI, without a corresponding increase in CCN-active particle number. This may artificially  
486 flatten the CER–AI and Nd–AI regression slopes, leading to apparently weaker ACI under moister  
487 conditions. Given that the SWMW and NEMW periods are characterized by substantially higher  
488 moisture levels than the NEMD period, the weaker ACI observed during these moister periods could  
489 partly reflect this hygroscopic swelling artifact rather than intrinsic differences in cloud microphysical  
490 sensitivity.

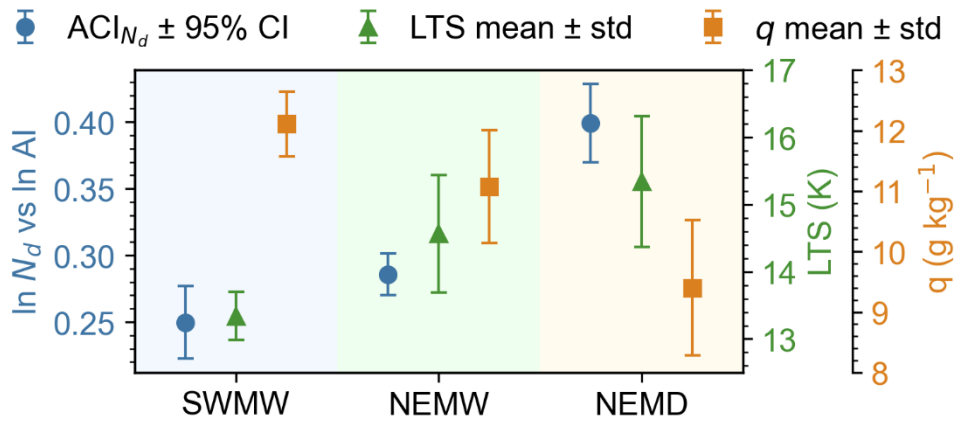
491 To assess whether the observed period-to-period differences are substantially affected by systematic  
492 humidity differences, we further stratified the data from each monsoon period into three RH ranges (0–  
493 45 %, 45–80 %, and 80–100 %). Under constrained LWP ( $50\text{--}200\text{ g m}^{-2}$ ) and cloud-top pressure (650–  
494 800 hPa) conditions,  $ACI_{Nd}$  was recalculated separately for each subsample. The RH used in this study  
495 is from ERA5 at 950 hPa at 06:00 UTC, representing the ambient environmental humidity within the  
496 marine atmospheric boundary layer. Previous studies show that aerosols are predominantly confined  
497 below  $\sim 3$  km in the marine atmosphere over the SCS (Li et al., 2020; Su et al., 2022), with a peak in  
498 extinction occurring at approximately  $\sim 480$  m (Su et al., 2022). Therefore, the 950 hPa RH is adopted as  
499 a representative proxy for the ambient humidity governing aerosol hygroscopic growth.

500 As shown in Table 2, the enhancement from SWMW to NEMW and further to NEMD is evident in the  
501 moderate and high RH bins (45–80 % and 80–100 %), whereas the low RH bin (0–45 %) does not exhibit  
502 statistically robust differences among the three periods. These results suggest that although AI may be  
503 affected by hygroscopic swelling under humid environments, this effect is insufficient to explain the  
504 systematic ACI differences among the three monsoon periods. Therefore, aerosol hygroscopic swelling  
505 is unlikely to be the dominant cause of the observed period-to-period variability, motivating further  
506 examination of the thermodynamic and moisture controls on ACI.

507 **Table 2:  $ACI_{Nd} \pm 95\%CI$  of deeper cumulus clouds under different relative humidity bins during the three**  
 508 **periods.**

Period	RH<45%	45% ≤ RH < 80%	80% ≤ RH ≤ 100%
SWMW	-0.126 ± 0.291	0.221 ± 0.043	0.278 ± 0.038
NEMW	-0.055 ± 0.194	0.262 ± 0.032	0.312 ± 0.018
NEMD	0.127 ± 0.102	0.371 ± 0.022	0.377 ± 0.012

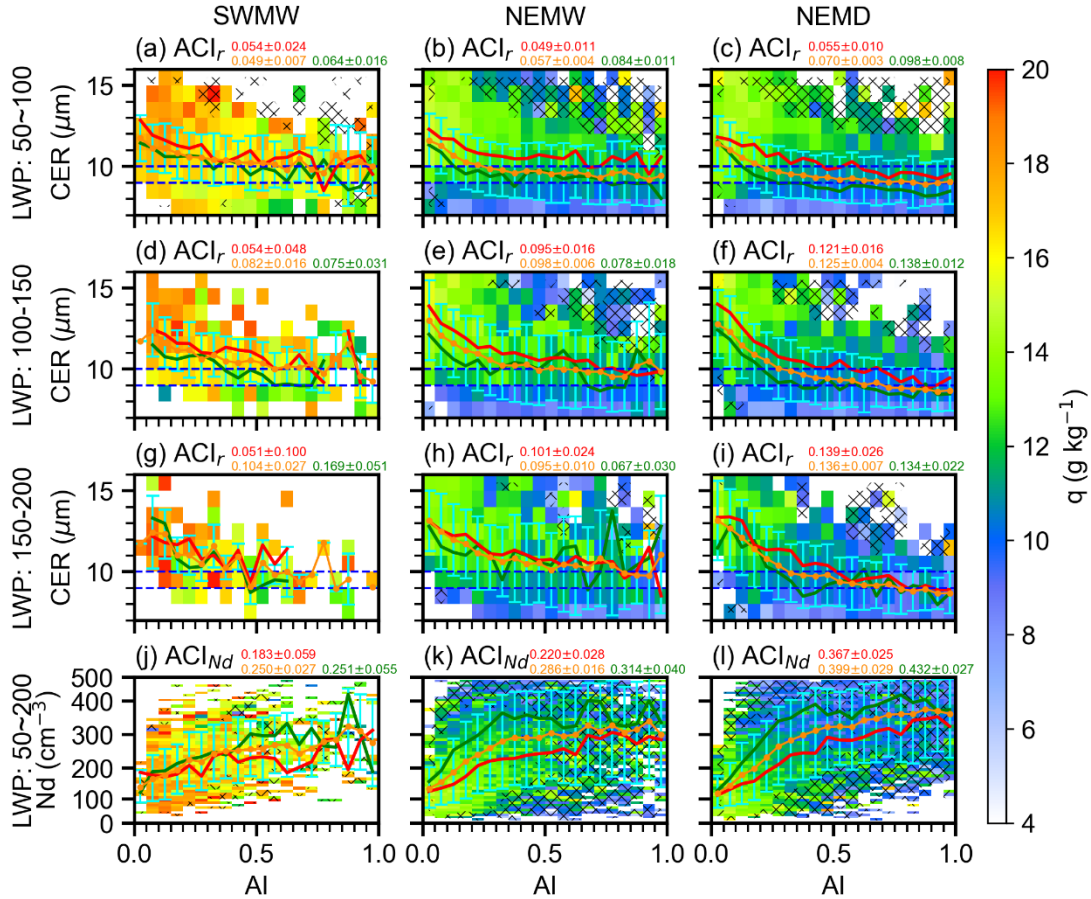
509 To provide an integrated view of how the ACI of deeper cumulus clouds co-varies with the  
 510 thermodynamic and moisture background across the three periods, Fig. 9 shows the  $ACI_{Nd}$  together with  
 511 the corresponding  $q$  and LTS. Both  $ACI_{Nd}$  and the key environmental regulators display a coherent  
 512 evolution across the three periods. From the SWMW to the NEMW and NEMD,  $ACI_{Nd}$  intensify steadily,  
 513 in parallel with declining moisture and increasing LTS. Quantitatively, The  $ACI_{Nd}$  increases  
 514 progressively from  $0.250 \pm 0.027$  (95% confidence interval, 95% CI) during the SWMW period to  $0.286$   
 515  $\pm 0.016$  during NEMW and further to  $0.399 \pm 0.029$  during NEMD. Meanwhile,  $q$  decreases from  $12.111$   
 516  $\pm 0.540$  g kg<sup>-1</sup> during SWMW to  $11.072 \pm 0.931$  g kg<sup>-1</sup> during NEMW and  $9.540 \pm 1.120$  g kg<sup>-1</sup> during  
 517 NEMD, while the LTS increases from  $13.341 \pm 0.358$  K to  $14.565 \pm 0.875$  K and  $15.343 \pm 0.977$  K,  
 518 respectively. (All  $q$  and LTS uncertainties represent one standard deviation, std.) These co-varying  
 519 changes indicate that both  $q$  and LTS may regulate the strengthening of ACI across the three periods  
 520 over the SCS. In the following subsections, we separately examine the roles of  $q$  (Section 3.5.1) and LTS  
 521 (Section 3.5.2) in regulating ACI.



522  
 523 **Figure 9:  $ACI_{Nd}$ , specific humidity ( $q$ ), and lower-tropospheric stability (LTS) for the three periods over the**  
 524 **South China Sea. The 95% confidence interval (CI) represents the uncertainty derived from the Student's t**  
 525 **test, whereas std denotes the one standard deviation.**

### 526 3.5.1 Water vapor

527 Water vapor supply substantially impacts CCN activation, droplet condensational growth, and  
528 coalescence, hence altering the cloud droplet size distribution (Feingold et al., 2006; Zheng et al., 2022).  
529 Specific humidity at 1000 hPa serves as a proxy for the ambient water vapor available to warm clouds,  
530 analogous to the use of near-surface specific humidity as a proxy for marine boundary layer moisture in  
531 previous studies (Dadashazar et al., 2020). To investigate the influence of water vapor on ACI in deeper  
532 cumulus clouds, specific humidity was averaged within each AI-CER/ $N_d$  interval separately for each  
533 period (Fig. 10). For each AI interval, CER/ $N_d$  was further averaged, and samples were stratified by the  
534 25th and 75th percentiles of specific humidity to represent dry (< 25th percentile) and moist (> 75th  
535 percentile) conditions, under which the corresponding mean CER/ $N_d$  was calculated. In addition, ACI  
536 was derived from all samples and separately for the dry and moist subsets in each period. To satisfy the  
537 LWP constraint required for the CER–AI analysis, the influence of water vapor on ACI was examined  
538 within LWP intervals of 50–100, 100–150, and 150–200 g m<sup>-2</sup>. In addition, because the  $N_d$ –AI  
539 relationship does not require an explicit LWP constraint for ACI <sub>$N_d$</sub>  calculation, it was examined over the  
540 broader LWP range of 50–200 g m<sup>-2</sup>.



541

542 **Figure 10: Influence of water vapor on ACI in deeper cumulus clouds (CTP: 650-800 hPa) across the three**  
 543 **periods. Rows 1–3 show mean specific humidity in CER–AI bins for LWP ranges of 50–100, 100–150, and**  
 544 **150–200 g m<sup>-2</sup>, respectively; row 4 shows mean specific humidity in N<sub>d</sub>–AI bins for LWP 50–200 g m<sup>-2</sup>.**  
 545 **Columns correspond to the southwest monsoon, northeast monsoon wet period, and northeast monsoon dry**  
 546 **period. Yellow dashed, red, and green lines denote the mean CER (rows 1–3) or N<sub>d</sub> (row 4) in each AI bin for**  
 547 **all samples, for moist conditions (specific humidity > 75th percentile), and for dry conditions (specific**  
 548 **humidity < 25th percentile), respectively. Error bars indicate the standard deviation of CER (rows 1–3) or**  
 549 **N<sub>d</sub> (row 4) within each AI bin. Yellow numbers indicate ACI ± 95% uncertainty estimates (according to a**  
 550 **Student’s t test) for all samples, whereas red and green numbers indicate the corresponding estimates under**  
 551 **moist and dry conditions, respectively.**

552 As shown in Fig. 10, higher specific humidity conditions are generally associated with larger CER and  
 553 lower N<sub>d</sub> across the three periods over the SCS. This may suggest that abundant water vapor enhances  
 554 condensational growth of cloud droplets, and the enlarged droplets are more susceptible to collision-  
 555 coalescence, which not only reduces N<sub>d</sub> but also further increases the CER. By contrast, under limited  
 556 water vapor availability, the ability of CCN-activated droplets to grow by condensation is substantially  
 557 constrained. The lack of a sufficient number of larger droplets favors condensation as the predominant  
 558 growth mechanism, thereby yielding smaller droplet sizes (Zheng et al., 2022).

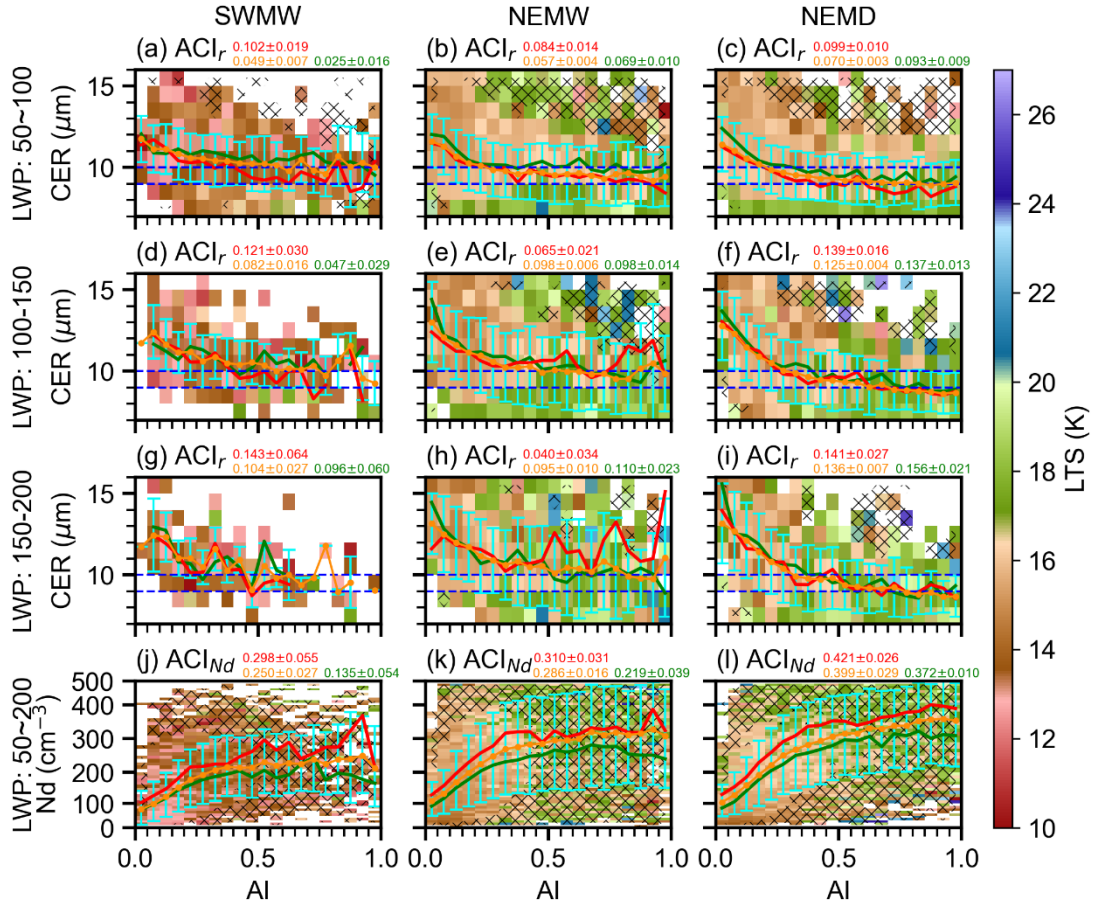
559 The response of ACI to environmental water availability exhibits different behaviors. Qiu et al. (2017)  
560 analysed the AI-CER relationship for non-raining warm clouds over the Southern Great Plains and found  
561 the anti-Twomey effect under moist conditions. Zheng et al. (2022) investigated non-raining warm  
562 clouds over the Eastern North Atlantic and found that sufficient water vapor availability can enhance  
563 ACI. Over the SCS, within the LWP range of 50–200 g m<sup>-2</sup>, ACI<sub>Nd</sub> is consistently smaller under moist  
564 conditions than under dry conditions across all three periods (Figs. 10j–l), suggesting that N<sub>d</sub> exhibits  
565 weaker sensitivity to aerosol perturbations in moist environments compared to dry environments. Figs.  
566 10j–l show that N<sub>d</sub> exhibits comparable values between moist and dry conditions at very low aerosol  
567 loading. As aerosol concentration increases, however, N<sub>d</sub> becomes smaller under moist conditions  
568 relative to dry conditions. This pattern may indicate that under ample water vapor availability, increased  
569 aerosol loading initially enhances cloud droplet activation, leading to elevated droplet number  
570 concentrations. But subsequent collision-coalescence promotes droplet growth while reducing N<sub>d</sub>.  
571 Consequently, the microphysical adjustments associated with enhanced moisture availability dampen the  
572 sensitivities of N<sub>d</sub> to aerosol perturbations, manifesting as weaker ACI<sub>Nd</sub> in the moist regime.

573 In contrast, the response of ACI<sub>r</sub> to moisture exhibits a dependence on LWP. At low LWP (50–100 g m<sup>-2</sup>)  
574 <sup>2</sup>, ACI<sub>r</sub> is reduced under moist relative to dry conditions across all periods (Figs. 10a–c). At higher LWP  
575 ranges, this reduction appears only in the Southwest Monsoon period within the 100–150 g m<sup>-2</sup> and 150–  
576 200 g m<sup>-2</sup> bins, and in the Northeast Monsoon Dry period within the 100–150 g m<sup>-2</sup> bin (Fig. 10g), while  
577 the opposite response is observed in other cases. The LWP is defined as the column-integrated liquid  
578 water content within clouds (e.g., existing cloud droplets) (Lee and Penner, 2011). At low LWP, ACI<sub>r</sub> is  
579 weaker under moist conditions (as indicated by 1000-hPa specific humidity) compared to dry conditions  
580 (Figs. 10a–c). A possible explanation is that in moist environments, enhanced collision-coalescence  
581 processes promote droplet growth, leading to larger CER. In contrast, under drier conditions, limited  
582 water vapor availability inhibits droplet growth, resulting in smaller CER. At higher LWP, when the in-  
583 cloud liquid water content is abundant, the response of ACI<sub>r</sub> to environmental water vapor variations  
584 becomes less consistent (Figs. 10d–i), suggesting the involvement of additional microphysical or  
585 dynamical processes.

586 Over the SCS, CER and Nd exhibit comparable values across the three periods within the same LWP  
587 interval at low AI. As AI increases, noticeable differences develop, with CER decreasing progressively  
588 from the SW to the NEMW and further to the NEMD, while Nd increases accordingly (Fig. 10).  
589 Consequently, ACI is enhanced stepwise from SW to NEMW and then to NEMD. This stepwise  
590 enhancement may be partly attributed to the progressive decrease in environmental water vapor from  
591 SW to NEMW and further to NEMD (Figs. 4a–c), particularly evident within the LWP interval of 50–  
592 100 g m<sup>-2</sup>.

### 593 **3.5.2 lower tropospheric stability**

594 Thermodynamic and dynamic conditions are key factors influencing aerosol vertical transport, aerosol  
595 activation processes, and cloud droplet formation. Thermodynamic stability can be quantitatively  
596 represented by the lower tropospheric stability (LTS), a measure of temperature inversion strength  
597 initially defined for marine stratocumulus clouds (Klein and Hartmann, 1993). This metric has been  
598 widely utilized to evaluate atmospheric stability and vertical mixing across both oceanic and continental  
599 regions (Jia et al., 2019; Ma et al., 2018b). Higher LTS values represent enhanced lower tropospheric  
600 stability, which suppresses vertical mixing and convective initiation. To further examine the influence of  
601 thermodynamic conditions on ACI in deeper cumulus clouds, the LTS was analysed in a manner identical  
602 to that used for specific humidity. For each period, samples were stratified by the 25th and 75th  
603 percentiles of LTS to represent unstable and stable conditions, respectively, and ACI was computed for  
604 each subset (Fig. 11). The analysis was performed within LWP intervals of 50–100, 100–150, and 150–  
605 200 g m<sup>-2</sup> for the CER–AI relationship, and over 50–200 g m<sup>-2</sup> for the Nd–AI relationship. Fig. 11 shows  
606 that stronger lower tropospheric stability (higher LTS) is associated with smaller CER and higher Nd, as  
607 enhanced static stability may suppresses convective mixing and vertical moisture transport, thereby  
608 limiting droplet growth while favouring higher droplet concentrations.



609

610 **Figure 11: Same as Fig. 10, but for lower tropospheric stability. Stable and unstable conditions correspond to**  
 611 **the upper (> 75th percentile) and lower (< 25th percentile) quartiles of LTS, respectively. Yellow numbers**  
 612 **indicate  $ACI \pm 95\%$  uncertainty estimates (according to a Student's t test) for all samples, whereas red and**  
 613 **green numbers indicate the corresponding estimates under stable and unstable conditions, respectively.**

614 In contrast to unstable conditions, stronger  $ACI_{Nd}$  is observed under stable conditions characterized by  
 615 higher LTS values (Figs. 11j–l). This suggests that enhanced LTS may be associated with environmental  
 616 conditions that influence ACI. Under more stable stratification, reduced vertical mixing may help  
 617 maintain higher aerosol concentrations and moisture within the boundary layer, which may in turn  
 618 influence cloud droplet activation and cloud microphysical properties. As a result, higher  $ACI_{Nd}$  is  
 619 observed under stable conditions compared to unstable environments. Over the SCS, LTS is generally  
 620 weaker during the southwest monsoon than during the northeast monsoon (Fig. 11), which may partly  
 621 contribute to the observed inter-monsoon differences in ACI. However, given the complexity of  
 622 concurrent variations in moisture, aerosol loading, and cloud regimes, the specific role of LTS in  
 623 modulating ACI cannot be isolated.

624 The response of  $ACI_r$  to LTS exhibits distinct behaviours across different LWP intervals and periods  
625 (Figs. 11a–i). During the southwest monsoon period,  $ACI_r$  is consistently larger under stable conditions  
626 than under unstable conditions across all three LWP ranges, consistent with the  $ACI_{Nd}$  results. However,  
627 during the northeast monsoon wet period, this enhancement is only evident in the lowest LWP range  
628 (50–100  $g\ m^{-2}$ ). In the northeast monsoon dry period, the enhancement under stable conditions is  
629 observed in both the 50–100  $g\ m^{-2}$  and 100–150  $g\ m^{-2}$  bins. This contrasting behaviour (Figs. 11e, h, i)  
630 can be further understood from the AI-CER relationships. At low AI values, corresponding to relatively  
631 clean conditions, CER is larger under unstable conditions than under stable conditions. As AI increases,  
632 indicating more polluted environments, CER under stable and unstable conditions gradually converges,  
633 leading to stronger  $ACI_r$  under unstable conditions. This pattern may indicate that during the northeast  
634 monsoon period, when in-cloud water vapor is abundant and aerosol loading is relatively high, cloud  
635 microphysical processes become less sensitive to variations in LTS. The inherently strong and weakly  
636 variable lower-tropospheric stability during the northeast monsoon may suppress the dynamical  
637 influence of further LTS changes  $ACI$ , thereby weakening the LTS dependence of  $ACI_r$  under moist and  
638 polluted conditions.

#### 639 **4 discussion and conclusions**

640 To investigate how  $ACI$  vary under the alternating influence of two opposing monsoon systems over the  
641 South China Sea (SCS) and how different environmental conditions modulate these interactions, the  
642 study period was divided into three representative phases based on variations in wind direction,  
643 precipitation, and specific humidity: the southwest monsoon wet period (SWMW), the northeast  
644 monsoon wet period (NEMW), and the northeast monsoon dry period (NEMD). Satellite observations  
645 and reanalysis data were used to quantify  $ACI$  variability and its environmental controls across different  
646 thermodynamic and moisture conditions.

647 Distinct environmental regimes characterize the three monsoon phases. SWMW is dominated by strong  
648 ascent, high SST, and abundant moisture. NEMW features enhanced continental aerosol transport,  
649 reduced SST, and increased LTS. NEMD is the driest and most stable regime, with widespread  
650 subsidence and favourable conditions for boundary-layer aerosol accumulation.

651 A pronounced Twomey effect was consistently identified across all three periods, as indicated by smaller  
652 CER and higher Nd with increasing aerosol loading under nearly constant LWP. Quantitative estimates  
653 of  $ACI_r$  show that the Twomey effect dominates when LWP ranges from 50 to 200 g m<sup>-2</sup>, whereas an  
654 apparent “anti-Twomey” behaviour appears in optically thin clouds (LWP < 50 g m<sup>-2</sup>), likely associated  
655 with strong competition for limited water vapor and entrainment-induced drying. Precipitation tends to  
656 amplify the ACI by simultaneously suppressing cloud droplet number concentrations and removing  
657 aerosols from the atmosphere. After removing raining samples, the ACI derived from non-raining warm  
658 clouds provides a more reliable representation of the first aerosol indirect effect, reducing biases caused  
659 by precipitation processes, although some uncertainty may remain due to undetected light precipitation  
660 under high-LWP conditions. Across the three periods, shallow stratocumulus clouds (CTP: 800–950 hPa)  
661 show limited variability in ACI, while deeper cumulus clouds (CTP: 650–800 hPa) exhibit the strongest  
662 ACI during NEMD. In contrast, no clear separation is observed between the SWMW and NEMW  
663 periods.

664 The inter-monsoon differences in deeper cumulus cloud ACI are primarily governed by coupled  
665 variations in moisture, atmospheric stability, and aerosol conditions rather than monsoon phase itself.  
666 Stronger ACI in NEMD is consistent with drier and more stable conditions that favour aerosol  
667 accumulation and suggests a possible role of aerosol accumulation in increasing aerosol availability for  
668 cloud activation, which may in turn contribute to stronger ACI. In contrast, moist and convectively active  
669 environments during SWMW and NEMW likely weaken ACI through enhanced condensational and  
670 coalescence growth processes. These results highlight the key role of environmental modulation in  
671 shaping the expression of the Twomey effect in marine warm clouds over the SCS.

672 Uncertainties arise from the use of AI as a proxy for CCN, which does not fully capture coarse-mode  
673 sea-salt aerosols, potential biases associated with aerosol hygroscopic growth, and assumptions in Nd  
674 retrieval (e.g., constant sub-adiabatic factor). Cloud selection criteria may preferentially retain more  
675 homogeneous scenes, potentially underrepresenting broken cumulus clouds, and may be less reliable for  
676 deeper trade cumulus and congestus clouds that dominate the 650–800 hPa CTP regime highlighted in  
677 this study. Undetected light precipitation may also affect ACI estimates, especially at high LWP. In  
678 addition, the present analysis cannot fully disentangle the respective influences of water vapor,

679 thermodynamic stability, cloud regime, and aerosol type and loading, as these factors co-vary  
680 systematically with the monsoon phase, which limits attribution of the observed inter-period ACI  
681 differences to any single controlling mechanism.

682 Despite these uncertainties, the results show that deeper cumulus cloud ACI over the SCS are strongly  
683 regulated by coupled variations in moisture, stability, and aerosol conditions associated with monsoon  
684 transitions. Monsoon phases act not as direct physical drivers but as an organizing framework for  
685 environmental variability that shapes cloud microphysical responses. Future work will focus on reducing  
686 observational and retrieval uncertainties to improve the quantification of ACI across different monsoon  
687 regimes. These findings provide important observational evidence for understanding ACI and offer  
688 valuable guidance for improving the representation of ACI in climate and numerical weather prediction  
689 models.

690

#### 691 Financial support

692 This work was supported by the National Natural Science Foundation of China (grant nos. 42027804,  
693 41775026, and 41075012). Hailing Jia was support by the project ACIaction (File No.  
694 OCENW.M.24.024) financed by the Dutch Research Council (NWO) under the grant  
695 <https://doi.org/10.61686/OZRJI30024>.

696

#### 697 Acknowledgements

698 Data and samples were collected onboard of R/V Shiyan 6 implementing the open research cruise  
699 NORC2024-07 supported by NSFC Shiptime Sharing Project (project number: 42349907). And we  
700 sincerely appreciate the valuable comments provided by the two anonymous reviewers, which  
701 significantly enhanced the clarity and robustness of this work.

702

#### 703 Competing Interest

704 The authors declare that they have no known competing financial interests or personal relationships that  
705 could have appeared to influence the work reported in this paper.

706

707 Author contributions

708 YL analysed the data and wrote the manuscript. HJ participated in scientific discussions and reviewed  
709 and refined the manuscript. YH participated in scientific discussions, and Resources, Project  
710 administration, Funding acquisition, Conceptualization, Formal analysis, Methodology, Writing –  
711 review & editing.

712

713 Data Availability

714 Atmospheric fields were obtained from the ERA5 reanalysis datasets produced by the European Centre  
715 for Medium-Range Weather Forecasts (ECMWF) via the Copernicus Climate Change Service (C3S)  
716 Climate Data Store (CDS). The data are publicly available at <https://cds.climate.copernicus.eu/>.

717 Aerosol datasets were obtained from the Modern-Era Retrospective Analysis for Research and  
718 Applications Version 2 (MERRA-2), produced by the NASA Goddard Earth Observing System (GEOS)  
719 Global Modeling and Assimilation Office (GMAO) and distributed by the Goddard Earth Sciences Data  
720 and Information Services Center (GES DISC). The data are publicly available at  
721 <https://disc.gsfc.nasa.gov/datasets?project=MERRA-2>.

722 Cloud retrievals were obtained from the Clouds and the Earth's Radiant Energy System (CERES)-  
723 Moderate Resolution Imaging Spectroradiometer (MODIS) Edition 4 Single Scanner Footprint (SSF)  
724 daily Level-3 products ( $1^\circ \times 1^\circ$  grid), produced by NASA's Langley Research Center (LaRC) and  
725 distributed by the Atmospheric Science Data Center (ASDC). The CERES–MODIS data are publicly  
726 available through the NASA ASDC archive at <https://ceres.larc.nasa.gov/data/#ssf1deg-level-3>.

727 Cloud droplet number concentration data are from Gryspeerdt et al. (2022) MODIS-based product ( $1^\circ \times$   
728  $1^\circ$ ), available at <https://dx.doi.org/10.5285/864a46cc65054008857ee5bb772a2a2b>

729 Sea surface temperature (SST) data were obtained from the National Oceanic and Atmospheric  
730 Administration (NOAA) Optimum Interpolation (OI) SST, Version 2, produced by the NOAA Physical  
731 Sciences Laboratory. The data are publicly available through the NOAA Physical Sciences Laboratory  
732 at <https://psl.noaa.gov/data/gridded/data.noaa.oisst.v2.html>.

733 IMERG V07 precipitation data used in this study are openly available from the NASA Goddard Earth  
734 Sciences Data and Information Services Center (GES DISC) at  
735 <https://disc.gsfc.nasa.gov/datasets?keywords=gpm%20imerg%2007>, as cited in Huffman et al. (2024).

736

## 737 **References**

738 Ackerman, A. S., Kirkpatrick, M. P., Stevens, D. E., and Toon, O. B.: The impact of humidity above  
739 stratiform clouds on indirect aerosol climate forcing, *Nature*, 432, 1014–1017,  
740 <https://doi.org/10.1038/nature03174>, 2004.

741 Albrecht, B. A.: Aerosols, Cloud Microphysics, and Fractional Cloudiness, *Science*, 245, 1227–1230,  
742 1989.

743 Bellouin, N., Quaas, J., Gryspeerdt, E., Kinne, S., Stier, P., Watson-Parris, D., Boucher, O., Carslaw, K.  
744 S., Christensen, M., Daniaou, A.-L., Dufresne, J.-L., Feingold, G., Fiedler, S., Forster, P., Gettelman, A.,  
745 Haywood, J. M., Lohmann, U., Malavelle, F., Mauritsen, T., McCoy, D. T., Myhre, G., Mülmenstädt, J.,  
746 Neubauer, D., Possner, A., Rugenstein, M., Sato, Y., Schulz, M., Schwartz, S. E., Sourdeval, O.,  
747 Storelvmo, T., Toll, V., Winker, D., and Stevens, B.: Bounding Global Aerosol Radiative Forcing of  
748 Climate Change, *Reviews of Geophysics*, 58, e2019RG000660, <https://doi.org/10.1029/2019RG000660>,  
749 2020.

750 Chen, J. and Hu, Z.: Seasonal variability in spatial patterns of sea surface cold- and warm fronts over the  
751 continental shelf of the northern South China Sea, *Front. Mar. Sci.*, 9,  
752 <https://doi.org/10.3389/fmars.2022.1100772>, 2023.

753 Chen, Y., Luo, T., Sun, G., Zhu, W., Liu, Q., Liu, Y., Jin, X., and Weng, N.: A Comprehensive Ensemble  
754 Model for Marine Atmospheric Boundary-Layer Prediction in Meteorologically Sparse and Complex  
755 Regions: A Case Study in the South China Sea, *Remote Sensing*, 17, 2046,  
756 <https://doi.org/10.3390/rs17122046>, 2025.

757 Chen, Y.-C., Christensen, M. W., Stephens, G. L., and Seinfeld, J. H.: Satellite-based estimate of global  
758 aerosol–cloud radiative forcing by marine warm clouds, *Nature Geosci*, 7, 643–646,  
759 <https://doi.org/10.1038/ngeo2214>, 2014.

760 Costantino, L. and Bréon, F.-M.: Aerosol indirect effect on warm clouds over South-East Atlantic, from  
761 co-located MODIS and CALIPSO observations, *Atmospheric Chemistry and Physics*, 13, 69–88,  
762 <https://doi.org/10.5194/acp-13-69-2013>, 2013.

763 Dadashazar, H., Crosbie, E., Majdi, M. S., Panahi, M., Moghaddam, M. A., Behrangi, A., Brunke, M.,  
764 Zeng, X., Jonsson, H. H., and Sorooshian, A.: Stratocumulus cloud clearings: statistics from satellites,

765 reanalysis models, and airborne measurements, *Atmos Chem Phys*, 20, 4637–4665,  
766 <https://doi.org/10.5194/acp-20-4637-2020>, 2020.

767 Dagan, G., Koren, I., Altaratz, O., and Heiblum, R. H.: Time-dependent, non-monotonic response of  
768 warm convective cloud fields to changes in aerosol loading, *Atmospheric Chemistry and Physics*, 17,  
769 7435–7444, <https://doi.org/10.5194/acp-17-7435-2017>, 2017.

770 Dezfuli, A. K., Ichoku, C. M., Huffman, G. J., Mohr, K. I., Selker, J. S., Van De Giesen, N.,  
771 Hochreutener, R., and Annor, F. O.: Validation of IMERG Precipitation in Africa, *Journal of*  
772 *Hydrometeorology*, 18, 2817–2825, <https://doi.org/10.1175/JHM-D-17-0139.1>, 2017.

773 Douglas, A. and L’Ecuyer, T.: Quantifying variations in shortwave aerosol–cloud–radiation interactions  
774 using local meteorology and cloud state constraints, *Atmospheric Chemistry and Physics*, 19, 6251–  
775 6268, <https://doi.org/10.5194/acp-19-6251-2019>, 2019.

776 Douville, H., Raghavan, K., Renwick, J., Allan, R. P., Arias, P. A., Barlow, M., Cerezo-Mota, R.,  
777 Cherchi, A., Gan, T. Y., and Gergis, J.: *Climate Change 2021 – The Physical Science Basis: Working*  
778 *Group I Contribution to the Sixth Assessment Report of the Intergovernmental Panel on Climate Change*,  
779 1st ed., Cambridge University Press, <https://doi.org/10.1017/9781009157896>, 2023.

780 Durden, S. L.: Evaluation of IMERG Data over Open Ocean Using Observations of Tropical Cyclones,  
781 *Remote Sensing*, 16, 2028, <https://doi.org/10.3390/rs16112028>, 2024.

782 Fan, J., Yuan, T., Comstock, J. M., Ghan, S., Khain, A., Leung, L. R., Li, Z., Martins, V. J., and  
783 Ovchinnikov, M.: Dominant role by vertical wind shear in regulating aerosol effects on deep convective  
784 clouds, *Journal of Geophysical Research: Atmospheres*, 114, <https://doi.org/10.1029/2009JD012352>,  
785 2009.

786 Fan, J., Wang, Y., Rosenfeld, D., and Liu, X.: Review of Aerosol–Cloud Interactions: Mechanisms,  
787 Significance, and Challenges, <https://doi.org/10.1175/JAS-D-16-0037.1>, 2016.

788 Feingold, G., Remer, L. A., Ramaprasad, J., and Kaufman, Y. J.: Analysis of smoke impact on clouds in  
789 Brazilian biomass burning regions: An extension of Twomey’s approach, *J. Geophys. Res.*, 106, 22907–  
790 22922, <https://doi.org/10.1029/2001JD000732>, 2001.

791 Feingold, G., Furrer, R., Pilewskie, P., Remer, L. A., Min, Q., and Jonsson, H.: Aerosol indirect effect  
792 studies at Southern Great Plains during the May 2003 Intensive Operations Period, *Journal of*  
793 *Geophysical Research: Atmospheres*, 111, <https://doi.org/10.1029/2004JD005648>, 2006.

794 Gelaro, R., McCarty, W., Suárez, M. J., Todling, R., Molod, A., Takacs, L., Randles, C. A., Darmenov,  
795 A., Bosilovich, M. G., Reichle, R., Wargan, K., Coy, L., Cullather, R., Draper, C., Akella, S., Buchard,  
796 V., Conaty, A., Silva, A. M. da, Gu, W., Kim, G.-K., Koster, R., Lucchesi, R., Merkova, D., Nielsen, J.  
797 E., Partyka, G., Pawson, S., Putman, W., Rienecker, M., Schubert, S. D., Sienkiewicz, M., and Zhao, B.:  
798 *The Modern-Era Retrospective Analysis for Research and Applications, Version 2 (MERRA-2)*,  
799 <https://doi.org/10.1175/JCLI-D-16-0758.1>, 2017.

800 Grosvenor, D. P., Sourdeval, O., Zuidema, P., Ackerman, A., Alexandrov, M. D., Bennartz, R., Boers,  
801 R., Cairns, B., Chiu, J. C., Christensen, M., Deneke, H., Diamond, M., Feingold, G., Fridlind, A.,  
802 Hünnerbein, A., Knist, C., Kollias, P., Marshak, A., McCoy, D., Merk, D., Painemal, D., Rausch, J.,  
803 Rosenfeld, D., Russchenberg, H., Seifert, P., Sinclair, K., Stier, P., van Dierenhoven, B., Wendisch, M.,  
804 Werner, F., Wood, R., Zhang, Z., and Quaas, J.: Remote Sensing of Droplet Number Concentration in  
805 Warm Clouds: A Review of the Current State of Knowledge and Perspectives, *Reviews of Geophysics*,  
806 56, 409–453, <https://doi.org/10.1029/2017RG000593>, 2018.

807 Gryspeerdt, E., Stier, P., White, B. A., and Kipling, Z.: Wet scavenging limits the detection of aerosol  
808 effects on precipitation, *Atmospheric Chemistry and Physics*, 15, 7557–7570,  
809 <https://doi.org/10.5194/acp-15-7557-2015>, 2015.

810 Gryspeerdt, E., Goren, T., Sourdeval, O., Quaas, J., Mülmenstädt, J., Dipu, S., Unglaub, C., Gettelman,  
811 A., and Christensen, M.: Constraining the aerosol influence on cloud liquid water path, *Atmospheric  
812 Chemistry and Physics*, 19, 5331–5347, <https://doi.org/10.5194/acp-19-5331-2019>, 2019.

813 Gryspeerdt, E., McCoy, D. T., Crosbie, E., Moore, R. H., Nott, G. J., Painemal, D., Small-Griswold, J.,  
814 Sorooshian, A., and Ziemba, L.: The impact of sampling strategy on the cloud droplet number  
815 concentration estimated from satellite data, *Atmospheric Measurement Techniques*, 15, 3875–3892,  
816 <https://doi.org/10.5194/amt-15-3875-2022>, 2022.

817 Hayden, L. J. M., Tan, J., Bolvin, D. T., and Huffman, G. J.: Variations in the Diurnal Cycle of  
818 Precipitation and Its Changes with Distance from Shore over Two Contrasting Regions as Observed by  
819 IMERG, ERA5, and Spaceborne Ku Radar, *Journal of Hydrometeorology*, 24, 675–689,  
820 <https://doi.org/10.1175/JHM-D-22-0154.1>, 2023.

821 Hersbach, H., Bell, B., Berrisford, P., Hirahara, S., Horányi, A., Muñoz-Sabater, J., Nicolas, J., Peubey,  
822 C., Radu, R., Schepers, D., Simmons, A., Soci, C., Abdalla, S., Abellan, X., Balsamo, G., Bechtold, P.,  
823 Biavati, G., Bidlot, J., Bonavita, M., De Chiara, G., Dahlgren, P., Dee, D., Diamantakis, M., Dragani, R.,  
824 Flemming, J., Forbes, R., Fuentes, M., Geer, A., Haimberger, L., Healy, S., Hogan, R. J., Hólm, E.,  
825 Janisková, M., Keeley, S., Laloyaux, P., Lopez, P., Lupu, C., Radnoti, G., De Rosnay, P., Rozum, I.,  
826 Vamborg, F., Villaume, S., and Thépaut, J.: The ERA5 global reanalysis, *Quart J Royal Meteor Soc*,  
827 146, 1999–2049, <https://doi.org/10.1002/qj.3803>, 2020.

828 Huffman, G. J., Bolvin, D. T., Braithwaite, D., Hsu, K.-L., Joyce, R. J., Kidd, C., Nelkin, E. J.,  
829 Sorooshian, S., Stocker, E. F., Tan, J., Wolff, D. B., and Xie, P.: Integrated Multi-satellite Retrievals for  
830 the Global Precipitation Measurement (GPM) Mission (IMERG), in: *Satellite Precipitation  
831 Measurement*, vol. 67, edited by: Levizzani, V., Kidd, C., Kirschbaum, D. B., Kummerow, C. D.,  
832 Nakamura, K., and Turk, F. J., Springer International Publishing, Cham, 343–353,  
833 [https://doi.org/10.1007/978-3-030-24568-9\\_19](https://doi.org/10.1007/978-3-030-24568-9_19), 2020.

834 Huffman, G. J., Bolvin, D. T., Braithwaite, D., Hsu, K., Joyce, R., Kidd, C., Nelkin, E., Sorooshian, S.,  
835 Tan, J., and Xie, P.: NASA Global Precipitation Measurement (GPM) Integrated Multi-Satellite

836 Retrievals for GPM (IMERG) Version 07, Algorithm Theoretical Basis Document (ATBD) Version, 47,  
837 2023.

838 Jia, H. and Quaas, J.: Nonlinearity of the cloud response postpones climate penalty of mitigating air  
839 pollution in polluted regions, *Nat. Clim. Chang.*, 13, 943–950, [https://doi.org/10.1038/s41558-023-](https://doi.org/10.1038/s41558-023-01775-5)  
840 01775-5, 2023.

841 Jia, H., Ma, X., Quaas, J., Yin, Y., and Qiu, T.: Is positive correlation between cloud droplet effective  
842 radius and aerosol optical depth over land due to retrieval artifacts or real physical processes?, *Atmos.*  
843 *Chem. Phys.*, 19, 8879–8896, <https://doi.org/10.5194/acp-19-8879-2019>, 2019.

844 Jia, H., Ma, X., Yu, F., and Quaas, J.: Significant underestimation of radiative forcing by aerosol–cloud  
845 interactions derived from satellite-based methods, *Nat Commun*, 12, 3649,  
846 <https://doi.org/10.1038/s41467-021-23888-1>, 2021.

847 Jia, H., Quaas, J., Gryspeerdt, E., Böhm, C., and Sourdeval, O.: Addressing the difficulties in quantifying  
848 droplet number response to aerosol from satellite observations, *Atmospheric Chemistry and Physics*, 22,  
849 7353–7372, <https://doi.org/10.5194/acp-22-7353-2022>, 2022.

850 Jia, H., Hasekamp, O., and Quaas, J.: Revisiting Aerosol–Cloud Interactions From Weekly Cycles,  
851 *Geophysical Research Letters*, 51, <https://doi.org/10.1029/2024gl108266>, 2024.

852 Jose, S., Nair, V. S., and Babu, S. S.: Anthropogenic emissions from South Asia reverses the aerosol  
853 indirect effect over the northern Indian Ocean, *Sci Rep*, 10, 18360, [https://doi.org/10.1038/s41598-020-](https://doi.org/10.1038/s41598-020-74897-x)  
854 74897-x, 2020.

855 Kim, B.-G., Schwartz, S. E., Miller, M. A., and Min, Q.: Effective radius of cloud droplets by ground-  
856 based remote sensing: Relationship to aerosol, *Journal of Geophysical Research: Atmospheres*, 108,  
857 <https://doi.org/10.1029/2003JD003721>, 2003.

858 Klein, S. A. and Hartmann, D. L.: *The Seasonal Cycle of Low Stratiform Clouds*, 1993.

859 Lee, S. S. and Penner, J. E.: Dependence of aerosol–cloud interactions in stratocumulus clouds on liquid-  
860 water path, *Atmospheric Environment*, 45, 6337–6346, <https://doi.org/10.1016/j.atmosenv.2011.08.050>,  
861 2011.

862 Lee, T.-W. and Park, J. E.: Thermodynamic correlations between the sea surface temperature, water  
863 vapor content, and cloud fraction, using MODIS data, *Theor Appl Climatol*, 150, 1699–1706,  
864 <https://doi.org/10.1007/s00704-022-04261-8>, 2022.

865 Li, Y., Wang, B., Lee, S.-Y., Zhang, Z., Wang, Y., and Dong, W.: Micro-Pulse Lidar Cruising  
866 Measurements in Northern South China Sea, *Remote Sensing*, 12, <https://doi.org/10.3390/rs12101695>,  
867 2020.

868 Liu, J., Yu, J., Lin, C., He, M., Liu, H., Wang, W., and Min, M.: Near-real-time atmospheric and oceanic  
869 science products of Himawari-8 and Himawari-9 geostationary satellites over the South China Sea, *Earth*  
870 *System Science Data*, 16, 4949–4969, <https://doi.org/10.5194/essd-16-4949-2024>, 2024.

871 Ma, P.-L., Rasch, P. J., Chepfer, H., Winker, D. M., and Ghan, S. J.: Observational constraint on cloud  
872 susceptibility weakened by aerosol retrieval limitations, *Nat Commun*, 9, 2640,  
873 <https://doi.org/10.1038/s41467-018-05028-4>, 2018a.

874 Ma, X., Jia, H., Yu, F., and Quaas, J.: Opposite Aerosol Index-Cloud Droplet Effective Radius  
875 Correlations Over Major Industrial Regions and Their Adjacent Oceans, *Geophysical Research Letters*,  
876 45, 5771–5778, <https://doi.org/10.1029/2018GL077562>, 2018b.

877 Martin, D. W. and Howland, M. R.: Rainfall over the Arabian Sea during the onset of the 1979 monsoon,  
878 *Nature*, 300, 628–630, <https://doi.org/10.1038/300628a0>, 1982.

879 McComiskey, A., Feingold, G., Frisch, A. S., Turner, D. D., Miller, M. A., Chiu, J. C., Min, Q., and  
880 Ogren, J. A.: An assessment of aerosol-cloud interactions in marine stratus clouds based on surface  
881 remote sensing, *J. Geophys. Res.*, 114, 2008JD011006, <https://doi.org/10.1029/2008JD011006>, 2009.

882 Miller, R. M., Rauber, R. M., Di Girolamo, L., Rilloraza, M., Fu, D., McFarquhar, G. M., Nesbitt, S. W.,  
883 Ziemba, L. D., Woods, S., and Thornhill, K. L.: Influence of natural and anthropogenic aerosols on cloud  
884 base droplet size distributions in clouds over the South China Sea and West Pacific, *Atmospheric*  
885 *Chemistry and Physics*, 23, 8959–8977, <https://doi.org/10.5194/acp-23-8959-2023>, 2023.

886 Minnis, P., Sun-Mack, S., Young, D. F., Heck, P. W., Garber, D. P., Chen, Y., Spangenberg, D. A.,  
887 Arduini, R. F., Trepte, Q. Z., Smith, W. L., Ayers, J. K., Gibson, S. C., Miller, W. F., Hong, G.,  
888 Chakrapani, V., Takano, Y., Liou, K.-N., Xie, Y., and Yang, P.: CERES Edition-2 Cloud Property  
889 Retrievals Using TRMM VIRS and Terra and Aqua MODIS Data—Part I: Algorithms, *IEEE*  
890 *Transactions on Geoscience and Remote Sensing*, 49, 4374–4400,  
891 <https://doi.org/10.1109/TGRS.2011.2144601>, 2011a.

892 Minnis, P., Sun-Mack, S., Chen, Y., Khaiyer, M. M., Yi, Y., Ayers, J. K., Brown, R. R., Dong, X.,  
893 Gibson, S. C., Heck, P. W., Lin, B., Nordeen, M. L., Nguyen, L., Palikonda, R., Smith, W. L.,  
894 Spangenberg, D. A., Trepte, Q. Z., and Xi, B.: CERES Edition-2 Cloud Property Retrievals Using  
895 TRMM VIRS and Terra and Aqua MODIS Data—Part II: Examples of Average Results and  
896 Comparisons With Other Data, *IEEE Transactions on Geoscience and Remote Sensing*, 49, 4401–4430,  
897 <https://doi.org/10.1109/TGRS.2011.2144602>, 2011b.

898 Minnis, P., Sun-Mack, S., Chen, Y., Chang, F.-L., Yost, C. R., Smith, W. L., Heck, P. W., Arduini, R.  
899 F., Bedka, S. T., Yi, Y., Hong, G., Jin, Z., Painemal, D., Palikonda, R., Scarino, B. R., Spangenberg, D.  
900 A., Smith, R. A., Trepte, Q. Z., Yang, P., and Xie, Y.: CERES MODIS Cloud Product Retrievals for  
901 Edition 4—Part I: Algorithm Changes, *IEEE Transactions on Geoscience and Remote Sensing*, 59,  
902 2744–2780, <https://doi.org/10.1109/TGRS.2020.3008866>, 2021.

903 Nakajima, T., Higurashi, A., Kawamoto, K., and Penner, J. E.: A possible correlation between satellite-  
904 derived cloud and aerosol microphysical parameters, *Geophysical Research Letters*, 28, 1171–1174,  
905 <https://doi.org/10.1029/2000GL012186>, 2001.

906 Ou, H., Cai, M., Zhang, Y., Ni, X., Liang, B., Sun, Q., Mai, S., Sun, C., Zhou, S., Wang, H., Sun, J., and  
907 Zhao, J.: Measurement report: Cloud condensation nuclei (CCN) activity in the South China Sea from  
908 shipborne observations during the summer and winter of 2021 – seasonal variation and anthropogenic  
909 influence, *Atmospheric Chemistry and Physics*, 25, 2495–2513, [https://doi.org/10.5194/acp-25-2495-](https://doi.org/10.5194/acp-25-2495-2025)  
910 2025, 2025.

911 Painemal, D.: Global estimates of changes in shortwave low-cloud albedo and fluxes due to variations  
912 in cloud droplet number concentration derived from CERES-MODIS satellite sensors, *Geophys Res Lett*,  
913 45, 9288–9296, <https://doi.org/10.1029/2018GL078880>, 2018.

914 Painemal, D., Chang, F.-L., Ferrare, R., Burton, S., Li, Z., Smith Jr., W. L., Minnis, P., Feng, Y., and  
915 Clayton, M.: Reducing uncertainties in satellite estimates of aerosol–cloud interactions over the  
916 subtropical ocean by integrating vertically resolved aerosol observations, *Atmospheric Chemistry and*  
917 *Physics*, 20, 7167–7177, <https://doi.org/10.5194/acp-20-7167-2020>, 2020.

918 Peng, S., Zhu, Y., Huang, K., Ding, X., Shi, R., Wu, D., Feng, Y., and Wang, D.: Detecting the structure  
919 of marine atmospheric boundary layer over the Northern South China Sea by shipboard GPS sondes,  
920 *Atmospheric Science Letters*, 17, 564–568, <https://doi.org/10.1002/asl.693>, 2016.

921 Qiu, Y., Zhao, C., Guo, J., and Li, J.: 8-Year ground-based observational analysis about the seasonal  
922 variation of the aerosol-cloud droplet effective radius relationship at SGP site, *Atmospheric*  
923 *Environment*, 164, 139–146, <https://doi.org/10.1016/j.atmosenv.2017.06.002>, 2017.

924 Randles, C. A., Silva, A. M. da, Buchard, V., Colarco, P. R., Darmenov, A., Govindaraju, R., Smirnov,  
925 A., Holben, B., Ferrare, R., Hair, J., Shinozuka, Y., and Flynn, C. J.: The MERRA-2 Aerosol Reanalysis,  
926 1980 Onward. Part I: System Description and Data Assimilation Evaluation,  
927 <https://doi.org/10.1175/JCLI-D-16-0609.1>, 2017.

928 Reynolds, R. W., Rayner, N. A., Smith, T. M., Stokes, D. C., and Wang, W.: An Improved In Situ and  
929 Satellite SST Analysis for Climate, 2002.

930 Rosenfeld, D., Zhu, Y., Wang, M., Zheng, Y., Goren, T., and Yu, S.: Aerosol-driven droplet  
931 concentrations dominate coverage and water of oceanic low-level clouds, *Science*, 363, eaav0566,  
932 <https://doi.org/10.1126/science.aav0566>, 2019.

933 Saponaro, G., Kolmonen, P., Sogacheva, L., Rodriguez, E., Virtanen, T., and De Leeuw, G.: Estimates  
934 of the aerosol indirect effect over the Baltic Sea region derived from 12 years of MODIS observations,  
935 *Atmos. Chem. Phys.*, 17, 3133–3143, <https://doi.org/10.5194/acp-17-3133-2017>, 2017.

936 Sato, Y., Goto, D., Michibata, T., Suzuki, K., Takemura, T., Tomita, H., and Nakajima, T.: Aerosol  
937 effects on cloud water amounts were successfully simulated by a global cloud-system resolving model,  
938 *Nat Commun*, 9, 985, <https://doi.org/10.1038/s41467-018-03379-6>, 2018.

939 Seinfeld, J. H., Bretherton, C., Carslaw, K. S., Coe, H., DeMott, P. J., Dunlea, E. J., Feingold, G., Ghan,  
940 S., Guenther, A. B., Kahn, R., Kraucunas, I., Kreidenweis, S. M., Molina, M. J., Nenes, A., Penner, J.  
941 E., Prather, K. A., Ramanathan, V., Ramaswamy, V., Rasch, P. J., Ravishankara, A. R., Rosenfeld, D.,  
942 Stephens, G., and Wood, R.: Improving our fundamental understanding of the role of aerosol–cloud  
943 interactions in the climate system, *Proceedings of the National Academy of Sciences*, 113, 5781–5790,  
944 <https://doi.org/10.1073/pnas.1514043113>, 2016.

945 Sorooshian, A., Anderson, B., Bauer, S. E., Braun, R. A., Cairns, B., Crosbie, E., Dadashazar, H., Diskin,  
946 G., Ferrare, R., Flagan, R. C., Hair, J., Hostetler, C., Jonsson, H. H., Kleb, M. M., Liu, H., MacDonald,  
947 A. B., McComiskey, A., Moore, R., Painemal, D., Russell, L. M., Seinfeld, J. H., Shook, M., Smith, W.  
948 L., Thornhill, K., Tselioudis, G., Wang, H., Zeng, X., Zhang, B., Ziemba, L., and Zuidema, P.: Aerosol–  
949 Cloud–Meteorology Interaction Airborne Field Investigations: Using Lessons Learned from the U.S.  
950 West Coast in the Design of ACTIVATE off the U.S. East Coast, [https://doi.org/10.1175/BAMS-D-18-](https://doi.org/10.1175/BAMS-D-18-0100.1)  
951 0100.1, 2019.

952 Stier, P., Van Den Heever, S. C., Christensen, M. W., Gryspeerdt, E., Dagan, G., Saleeby, S. M.,  
953 Bollasina, M., Donner, L., Emanuel, K., Ekman, A. M. L., Feingold, G., Field, P., Forster, P., Haywood,  
954 J., Kahn, R., Koren, I., Kummerow, C., L’Ecuyer, T., Lohmann, U., Ming, Y., Myhre, G., Quaas, J.,  
955 Rosenfeld, D., Samset, B., Seifert, A., Stephens, G., and Tao, W.-K.: Multifaceted aerosol effects on  
956 precipitation, *Nat. Geosci.*, 17, 719–732, <https://doi.org/10.1038/s41561-024-01482-6>, 2024.

957 Su, W., Loeb, N. G., Xu, K.-M., Schuster, G. L., and Eitzen, Z. A.: An estimate of aerosol indirect effect  
958 from satellite measurements with concurrent meteorological analysis, *Journal of Geophysical Research:*  
959 *Atmospheres*, 115, <https://doi.org/10.1029/2010JD013948>, 2010.

960 Su, Y., Han, Y., Luo, H., Zhang, Y., Shao, S., Xie, X., Su, Y., Han, Y., Luo, H., Zhang, Y., Shao, S., and  
961 Xie, X.: Physical-Optical Properties of Marine Aerosols over the South China Sea: Shipboard  
962 Measurements and MERRA-2 Reanalysis, *Remote Sensing*, 14, <https://doi.org/10.3390/rs14102453>,  
963 2022.

964 Sun, Q., Liang, B., Cai, M., Zhang, Y., Ou, H., Ni, X., Sun, X., Han, B., Deng, X., Zhou, S., and Zhao,  
965 J.: Cruise observation of the marine atmosphere and ship emissions in South China Sea: Aerosol  
966 composition, sources, and the aging process, *Environmental Pollution*, 316, 120539,  
967 <https://doi.org/10.1016/j.envpol.2022.120539>, 2023.

968 Tan, J., Huffman, G. J., Bolvin, D. T., and Nelkin, E. J.: Diurnal Cycle of IMERG V06 Precipitation,  
969 *Geophysical Research Letters*, 46, 13584–13592, <https://doi.org/10.1029/2019GL085395>, 2019a.

970 Tan, J., Huffman, G. J., Bolvin, D. T., and Nelkin, E. J.: IMERG V06: Changes to the Morphing  
971 Algorithm, <https://doi.org/10.1175/JTECH-D-19-0114.1>, 2019b.

972 Tu, Q., Zhao, Y., Guo, J., Cheng, C., Shi, L., Yan, Y., and Hao, Z.: Spatial and Temporal Variations of  
973 Aerosol Optical Thickness over the China Seas from Himawari-8, *Remote Sensing*, 13, 5082,  
974 <https://doi.org/10.3390/rs13245082>, 2021.

975 Twomey, S.: Pollution and the planetary albedo, *Atmospheric Environment* (1967), 8, 1251–1256,  
976 [https://doi.org/10.1016/0004-6981\(74\)90004-3](https://doi.org/10.1016/0004-6981(74)90004-3), 1974.

977 Twomey, S.: *The Influence of Pollution on the Shortwave Albedo of Clouds*, 1977.

978 Wall, C. J., Norris, J. R., Possner, A., McCoy, D. T., McCoy, I. L., and Lutsko, N. J.: Assessing effective  
979 radiative forcing from aerosol–cloud interactions over the global ocean, *Proceedings of the National  
980 Academy of Sciences*, 119, e2210481119, <https://doi.org/10.1073/pnas.2210481119>, 2022.

981 Wall, C. J., Storelvmo, T., and Possner, A.: Global observations of aerosol indirect effects from marine  
982 liquid clouds, *Atmospheric Chemistry and Physics*, 23, 13125–13141, [https://doi.org/10.5194/acp-23-  
983 13125-2023](https://doi.org/10.5194/acp-23-13125-2023), 2023.

984 Wang, B., LinHo, Zhang, Y., and Lu, M.-M.: Definition of South China Sea Monsoon Onset and  
985 Commencement of the East Asia Summer Monsoon, <https://doi.org/10.1175/2932.1>, 2004.

986 Wang, B., Huang, F., Wu, Z., Yang, J., Fu, X., and Kikuchi, K.: Multi-scale climate variability of the  
987 South China Sea monsoon: A review, *Dynamics of Atmospheres and Oceans*, 47, 15–37,  
988 <https://doi.org/10.1016/j.dynatmoce.2008.09.004>, 2009.

989 Wang, F., Guo, J., Wu, Y., Zhang, X., Deng, M., Li, X., Zhang, J., and Zhao, J.: Satellite observed  
990 aerosol-induced variability in warm cloud properties under different meteorological conditions over  
991 eastern China, *Atmospheric Environment*, 84, 122–132,  
992 <https://doi.org/10.1016/j.atmosenv.2013.11.018>, 2014.

993 Wang, J.-J., Li, X., and Carey, L. D.: Evolution, Structure, Cloud Microphysical, and Surface Rainfall  
994 Processes of Monsoon Convection during the South China Sea Monsoon Experiment, *Journal of the  
995 Atmospheric Sciences*, 64, 360–380, <https://doi.org/10.1175/JAS3852.1>, 2007.

996 Wang K.-Y., Sui C.-H., Lu M.-M., and Hong J.-S.: Cold Surge Impacts on the Structure, Energy Budget,  
997 and Turbulence of the South China Sea Boundary Layer, <https://doi.org/10.1175/MWR-D-23-0238.1>,  
998 2024a.

999 Wang, S., Wang, Q., and Feingold, G.: Turbulence, Condensation, and Liquid Water Transport in  
1000 Numerically Simulated Nonprecipitating Stratocumulus Clouds, 2003.

1001 Wang, Y., Zhao, P., Xiao, H., and Zhang, P.: Aerosol effects on liquid cloud microphysical properties in  
1002 south China: Land–ocean contrasts, *Atmospheric Pollution Research*, 15, 102032,  
1003 <https://doi.org/10.1016/j.apr.2023.102032>, 2024b.

1004 Wang, Y., Li, J., Fang, F., Zhang, P., He, J., Pöhlker, M. L., Henning, S., Tang, C., Jia, H., Wang, Y.,  
1005 Jian, B., Shi, J., and Huang, J.: In-situ observations reveal weak hygroscopicity in the Southern Tibetan

- 1006 Plateau: implications for aerosol activation and indirect effects, *npj Clim Atmos Sci*, 7, 77,  
1007 <https://doi.org/10.1038/s41612-024-00629-x>, 2024c.
- 1008 Wang, Y., Jia, H., Zhang, P., Fang, F., Li, J., Zhu, L., Wang, Y., Wang, T., and Li, J.: Sensitivity of cloud  
1009 microphysics to aerosol is highly associated with cloud water content: Implications for indirect radiative  
1010 forcing, *Atmospheric Research*, 309, 107552, <https://doi.org/10.1016/j.atmosres.2024.107552>, 2024d.
- 1011 Watters, D. and Battaglia, A.: The Summertime Diurnal Cycle of Precipitation Derived from IMERG,  
1012 *Remote Sensing*, 11, 1781, <https://doi.org/10.3390/rs11151781>, 2019.
- 1013 Watters, D., Battaglia, A., and Allan, R. P.: The Diurnal Cycle of Precipitation according to Multiple  
1014 Decades of Global Satellite Observations, Three CMIP6 Models, and the ECMWF Reanalysis, *Journal*  
1015 *of Climate*, 34, 5063–5080, <https://doi.org/10.1175/JCLI-D-20-0966.1>, 2021.
- 1016 Wu, Z., Jiang, C., Conde, M., Chen, J., and Deng, B.: The long-term spatiotemporal variability of sea  
1017 surface temperature in the northwest Pacific and China offshore, *Ocean Science*, 16, 83–97,  
1018 <https://doi.org/10.5194/os-16-83-2020>, 2020.
- 1019 Xiao, H.-W., Xiao, H.-Y., Luo, L., Shen, C.-Y., Long, A.-M., Chen, L., Long, Z.-H., and Li, D.-N.:  
1020 Atmospheric aerosol compositions over the South China Sea: temporal variability and source  
1021 apportionment, *Atmospheric Chemistry and Physics*, 17, 3199–3214, [https://doi.org/10.5194/acp-17-](https://doi.org/10.5194/acp-17-3199-2017)  
1022 [3199-2017](https://doi.org/10.5194/acp-17-3199-2017), 2017.
- 1023 Yost, C. R., Minnis, P., Sun-Mack, S., Chen, Y., and Smith, W. L.: CERES MODIS Cloud Product  
1024 Retrievals for Edition 4—Part II: Comparisons to CloudSat and CALIPSO, *IEEE Transactions on*  
1025 *Geoscience and Remote Sensing*, 59, 3695–3724, <https://doi.org/10.1109/TGRS.2020.3015155>, 2021.
- 1026 Yuan, C.-S., Chuang, H.-L., Tseng, Y.-L., Li, T.-C., Soong, K.-Y., and Cheng, W.-H.: Long-range  
1027 transport and source apportionment of marine fine particles in the Taiwan Strait and South China Sea  
1028 Intersection: Spatiotemporal variations and chemical fingerprints, *Atmospheric Environment*, 339,  
1029 120867, <https://doi.org/10.1016/j.atmosenv.2024.120867>, 2024.
- 1030 Yuan, T., Li, Z., Zhang, R., and Fan, J.: Increase of cloud droplet size with aerosol optical depth: An  
1031 observation and modeling study, *Journal of Geophysical Research: Atmospheres*, 113,  
1032 <https://doi.org/10.1029/2007JD008632>, 2008.
- 1033 Zhang, C., Xu, H., Li, Z., Xie, Y., and Li, D.: Maritime Aerosol Optical and Microphysical Properties in  
1034 the South China Sea Under Multi-source Influence, *Sci Rep*, 9, 17796, [https://doi.org/10.1038/s41598-](https://doi.org/10.1038/s41598-019-54483-6)  
1035 [019-54483-6](https://doi.org/10.1038/s41598-019-54483-6), 2019.
- 1036 Zhang, G. J., Ramanathan, V., and McPhaden, M. J.: Convection-Evaporation Feedback in the Equatorial  
1037 Pacific, 1995.

- 1038 Zhang, Y. and Wang, K.: The Changing Morphology of Global Precipitation Systems during the Last  
1039 Two Decades, *Bulletin of the American Meteorological Society*, 105, E1861–E1880,  
1040 <https://doi.org/10.1175/BAMS-D-23-0106.1>, 2024.
- 1041 Zhao, C., Sun, Y., Yang, J., Li, J., Zhou, Y., Yang, Y., Fan, H., and Zhao, X.: Observational evidence  
1042 and mechanisms of aerosol effects on precipitation, *Science Bulletin*, 69, 1569–1580,  
1043 <https://doi.org/10.1016/j.scib.2024.03.014>, 2024.
- 1044 Zheng, B., Qu, J., Huang, Y., Peng, D., Gu, D., Li, C., and Huang, R.: Evaluating the Seasonal Cycle of  
1045 the South China Sea Monsoon in CMIP6 Models, *J Meteorol Res*, 39, 322–337,  
1046 <https://doi.org/10.1007/s13351-025-4170-x>, 2025.
- 1047 Zheng, H., Liu, M., Lohmann, R., Li, D., Vojta, S., Katz, S., Wang, W., Ke, H., Wang, C., and Cai, M.:  
1048 Gaseous polycyclic aromatic hydrocarbons over the South China Sea: Implications for atmospheric  
1049 transport under monsoon influences, *Marine Pollution Bulletin*, 191, 114982,  
1050 <https://doi.org/10.1016/j.marpolbul.2023.114982>, 2023.
- 1051 Zheng, X., Xi, B., Dong, X., Wu, P., Logan, T., and Wang, Y.: Environmental effects on aerosol–cloud  
1052 interaction in non-precipitating marine boundary layer (MBL) clouds over the eastern North Atlantic,  
1053 *Atmos. Chem. Phys.*, 22, 335–354, <https://doi.org/10.5194/acp-22-335-2022>, 2022.
- 1054 Zhu, S., Xiao, Z., Che, H., and Chen, Q.: Impact of aerosols on warm clouds over the Sichuan Basin,  
1055 China in winter based on the MERRA-2 reanalysis dataset, *Atmospheric Pollution Research*, 13, 101342,  
1056 <https://doi.org/10.1016/j.apr.2022.101342>, 2022.
- 1057 Zhu, S., Li, Z., Chen, M., Wen, Y., Gao, S., Zhang, J., Wang, J., Nan, Y., Ferraro, S. C., Tsoodle, T. E.,  
1058 and Hong, Y.: How has the latest IMERG V07 improved the precipitation estimates and hydrologic  
1059 utility over CONUS against IMERG V06?, *Journal of Hydrology*, 645, 132257,  
1060 <https://doi.org/10.1016/j.jhydrol.2024.132257>, 2024.

1061